Monthly Notices of the ROYAL ASTRONOMICAL SOCIETY

MNRAS **433,** 2667–2692 (2013) doi:10.1093/mnras/stt947
Advance Access publication 2013 June 21

S0 galaxies in the Coma cluster: environmental dependence of the S0 offset from the Tully–Fisher relation

T. D. Rawle,[1★] John R. Lucey,[2] Russell J. Smith[2] and J. T. C. G. Head[2]

[1]*ESAC, ESA, Box 78, Villanueva de la Cañada, E-28691 Madrid, Spain*
[2]*Department of Physics, Durham University, South Road, Durham DH1 3LE, UK*

Accepted 2013 May 29. Received 2013 May 29; in original form 2013 April 29

ABSTRACT

We present deep Gemini Multi-Object Spectrograph long-slit spectroscopy of 15 Coma cluster S0 galaxies, and extract kinematic properties along the major axis to several times the disc scalelength. Supplementing our data set with previously published data, we create a combined sample of 29 Coma S0s, as well as a comparison sample of 38 Coma spirals. Using photometry from the Sloan Digital Sky Survey and Two Micron All Sky Survey, we construct the Tully–Fisher relation (TFR; luminosity versus maximum rotational velocity) for S0 galaxies. At fixed rotational velocity, the Coma S0 galaxies are on average fainter than Coma spirals by 1.10 ± 0.18, 0.86 ± 0.19 and 0.83 ± 0.19 mag in the g, i and K_s bands, respectively. The typical S0 offsets remain unchanged when calculated relative to large field-galaxy spiral samples. The observed offsets are consistent with a simple star formation model in which S0s are identical to spirals until abrupt quenching occurs at some intermediate redshift. The offsets form a continuous distribution tracing the time since the cessation of star formation, and exhibit a strong correlation ($>6\sigma$) with residuals from the optical colour–magnitude relation. Typically, S0s which are fainter than average for their rotational velocity are also redder than average for their luminosity. The S0 TFR offset is also correlated with both the projected cluster-centric radius and the Σ (projected) local density parameter. Since current local environment is correlated with time of accretion into the cluster, our results support a scenario in which transformation of spirals to S0s is triggered by cluster infall.

Key words: galaxies: clusters: individual: Coma – galaxies: elliptical and lenticular, cD – galaxies: stellar content.

1 INTRODUCTION

Galaxies are often separated into the categories ‘late-type’ and ‘early-type’, where the latter comprises both ellipticals and S0 (lenticular) galaxies. S0s observed to the half-light radius are typically dominated by the bulge, which is akin to a low-luminosity elliptical galaxy (Moorthy & Holtzman 2006; Thomas & Davies 2006; Morelli et al. 2008).

Although the stellar content of an S0 galaxy is broadly similar to a quiescent elliptical galaxy, the structure and kinematics are generally comparable to spiral galaxies (Bedregal et al. 2006a). If one turns off the star formation in a spiral galaxy, and within approximately 1–2 Gyr, an S0-like object is formed. With their spheroidal bulge and flat, mostly gas-free disc, S0s have long been postulated as a transitional stage between spiral and elliptical galaxies. Possible mechanisms for this transformation include minor mergers, slow encounters, harassment or some combination of these (Dressler & Sandage 1983; Neistein et al. 1999). However, as S0s make up the plurality of galaxies in rich local clusters (e.g. Dressler 1980b; Dressler et al. 1987), many evolutionary mechanisms have been proposed in which the star formation in a spiral has been abruptly truncated by processes specifically related to cluster infall (Gunn & Gott 1972; review in Boselli & Gavazzi 2006). Theories include starvation (removal of hot gas reservoirs via interaction with the intracluster medium; e.g. Larson, Tinsley & Caldwell 1980; McCarthy et al. 2008), tidally induced starbursts (Bekki 1999) and ram-pressure stripping of cold gas (Gunn & Gott 1972; Abadi, Moore & Bower 1999). However, if S0s are the direct descendants of objects analogous to local spirals, then for a common environment, the luminosity distribution of S0s would be systematically fainter than spirals. Instead, Burstein et al. (2005) and Sandage (2005) both showed that the typical surface brightness of S0s is greater than for spirals, and Dressler (1980b) suggested that the bulge luminosity of S0s is too large to evolve from spirals by disc fading alone (also Cortesi et al. 2013). The total luminosity and relative bulge mass of S0s could both increase if they were formed via minor mergers, harassment or tidally induced central starbursts (Christlein & Zabludoff 2004; Wilman et al. 2009).

★E-mail: tim.rawle@sciops.esa.int

At redshifts up to $z \sim 1$, Bundy et al. (2010) observed passive red spirals, likely to be the progenitors of the young S0s observed in nearby clusters. The existence of such galaxies suggests that transformations in colour and morphology occur at different epochs. For clusters at $z \sim 0.5$ (∼5 Gyr ago), Moran et al. (2007) and Geach et al. (2009) also report populations of transitionary objects likely to be in the process of converting from spiral to S0, while Rawle et al. (2012) discover cluster galaxies at $z \sim 0.3$ (∼3 Gyr ago) that appear to have undergone recent stripping of outer gas and dust. Additionally, Dressler et al. (1997) found that the fraction of S0s in rich clusters at $z \sim 0.5$ is two to three times smaller than in their local analogues, with a corresponding increase in the spiral fraction. These studies all imply that a large proportion of S0s were transformed from spirals over the last 5 Gyr. Poggianti et al. (2001) measured the stellar populations of a small sample of S0 galaxies in the nearby Coma cluster, finding that 40 per cent had indeed undergone star formation during the last ∼5 Gyr.

For spiral galaxies, the Tully–Fisher relation (TFR; Tully & Fisher 1977) is a tight empirical correlation between luminosity and the maximum rotational velocity. With large H I-based galaxy surveys (e.g. SFI++; Masters et al. 2006) and optical Hα rotation curve measurements (e.g. Courteau et al. 2007), the TFR for thousands of spirals has now been constructed. Such TFR studies regularly use imaging from the Sloan Digital Sky Survey (SDSS) to obtain homogeneous photometry (e.g Pizagno et al. 2007; Hall et al. 2012; Mocz et al. 2012). The spiral TFR exhibits a consistent intrinsic scatter throughout the optical bands 0.43 ± 0.03 mag in SDSS *griz* (e.g. Pizagno et al. 2007) and 0.41 mag in the I_C band (Tully & Courtois 2012).

Several studies have investigated the same relation for local S0s (Neistein et al. 1999; Bedregal, Aragón-Salamanca & Merrifield 2006b), and found that they have a systematic luminosity offset compared to the spiral population [in the B band: 1.7 ± 0.4 mag fainter compared to the Tully & Pierce (2000) TFR]. As truncation of star formation would fade the galaxy disc (by failing to replenish the population with young, luminous stars), this was advocated as evidence for disc fading, with the increased scatter in the relation interpreted as variation in the epoch of truncation. S0s form a continuum with other red spirals, which are also offset from the TFR (offset ∼0.5 mag for high-rotational-velocity Sa galaxies; Courteau et al. 2007; Pizagno et al. 2007). The intrinsic scatter of the S0 TFR is generally larger than that for spirals (0.6–0.8 mag; Bedregal et al. 2006b), which may reflect a more varied progenitor spiral population. Alternatively, the scatter may merely show that true S0s are difficult to isolate cleanly from red spirals.

The merger hypothesis struggles to explain the TFR offset unless the progenitor population was significantly different to spirals at $z = 0$ (Neistein et al. 1999). However, the TFR for S0s is still an area of controversy, with some studies (e.g. Hinz, Rieke & Caldwell 2003; Williams, Bureau & Cappellari 2009) reporting no discernible luminosity offset from spirals. These apparently support a variety of scenarios to form the heterogeneous set of S0s observed.

In order to investigate further the formation of S0s in the cluster environment, we have undertaken deep Gemini Multi-Object Spectrograph (GMOS) long-slit observations of 15 S0 galaxies in the Coma cluster, probing out to several disc scalelengths. Through a detailed exploration of bulge and disc properties, we aim to constrain the effect of local environment on galaxy evolution and discriminate between possible formation mechanisms.

In this paper, we introduce the observations (Section 2) and describe in detail the data reduction and derivation of kinematic properties (Section 3). We combine our data with previous Coma cluster S0 samples, and describe a carefully constructed Coma cluster spiral sample (Section 4). In Section 5, we calculate the S0 TFR, relative to both the Coma spirals and published TFRs which used large samples of spirals. We particularly concentrate on interpreting the environmental dependence of the S0-to-spiral offset. Section 6 summarizes our conclusions.

2 OBSERVATIONS

2.1 GMOS Coma cluster sample

The sample consists of 15 edge-on S0 galaxies in the nearby Coma cluster [Abell 1656; $z = 0.0231$, $\langle cz_{\rm cmb} \rangle = 7194\,{\rm km\,s^{-1}}$ from the NASA/IPAC Extragalactic Database[1] (NED)], as listed in Table 1. Each galaxy is a confirmed cluster member and was morphologically classified as an S0 by Dressler (1980a, hereafter D80).

Although the sample is not complete in any rigorous sense, the galaxies are selected to cover a range in luminosity (m_i = 12.5–15.0) and all lie on the red sequence (see Section 5.2.1). They are also located at a range of projected cluster radii (and hence a range of local densities), in order to probe the effect of local environment. Each S0 galaxy was examined in deep, optical imaging from MegaCam at the Canada–France–Hawaii Telescope (CFHT; g band shown in Fig. 1), and visually classified as an 'optimum' edge-on S0 by confirming a break in the smooth surface brightness profile. Many of the galaxies appear to have a prominent bulge and an extended disc with a g-band surface brightness $\mu_g > 22$ mag arcsec^{-2} (see Section 3.3 for the final bulge/disc decomposition).

Abundant ancillary data are available for each galaxy. In this paper, we use total magnitudes in g and i bands ($\lambda_{\rm obs}$ = 469, 748 nm) from the SDSS DR9 (Ahn et al. 2012) photoObj catalogue[2] (cModelMag parameter), and K_s band (2.16 μm) from the Two Micron All Sky Survey (2MASS) extended source catalogue[3] (XSC; Jarrett et al. 2000, k_m_ext parameter). Apparent magnitudes are listed in Table 1, and to facilitate comparison with previous studies, we quote AB mags for SDSS photometry and Vega mags for 2MASS.

2.2 GMOS observations

This investigation uses long-slit spectroscopy from GMOS (Hook et al. 2004) on the Gemini North telescope, Mauna Kea (programmes: GN-2009A-Q-52, PI: Lucey; GN-2011A-Q-50, PI: Rawle). In 2009, GMOS was operated with the B1200 grating and a 2 arcsec wide slit, resulting in a spectral resolution of 5.1 Å full width at half-maximum (FWHM). In 2011, we used the newly available B600 grating to increase the scheduling likelihood, and decreased the slit width to 1.5 arcsec, resulting in a spectral resolution of 8.5 Å FWHM. The full instrument configurations are summarized in Table 2.

Successful exploration of the disc-dominated region of these S0 galaxies relies on probing to a g-band surface brightness $\mu_g \sim$ 23 mag arcsec^{-2}. Derivation of reliable kinematics requires a signal-to-noise ratio (S/N) $\gtrsim 20$ Å^{-1}, while stellar population gradients (to be presented in a future paper) require S/N $\gtrsim 30$ Å^{-1}. To achieve this, we devoted 3 h of observing time to each target, with four exposures of 2380 s (9520 s in total) on-source. For each observation,

[1] http://ned.ipac.caltech.edu/
[2] Accessed via http://skyserver.sdss3.org/CasJobs/
[3] Accessed via http://irsa.ipac.caltech.edu/

Table 1. Observed parameters for the GMOS Coma cluster S0 galaxy sample, observed in 2009 and 2011. GMP ID from Godwin, Metcalfe & Peach (1983). Position (in decimal degrees), disc position angle (PA), g- and i-band total apparent magnitude (in AB magnitudes) are from SDSS. K_s-band total apparent magnitude (in Vega magnitudes) is extracted from 2MASS. Heliocentric velocity (cz_{hel}) and observed maximum rotation velocity (V_{obs}) measured as described in Section 3.4. GMP5160 was observed in both 2009 and 2011; kinematics derive from the latter data.

GMP ID	NGC #	RA J2000	Dec. J2000	PA (deg)	m_g (mag)	m_i (mag)	m_{K_s} (mag)	cz_{hel} (km s^{-1})	V_{obs} (km s^{-1})	Obs year
GMP1176	4931	195.753 65	28.032 47	78	13.796 ± 0.002	12.677 ± 0.002	10.31 ± 0.03	5364	192 ± 5	09
GMP1504		195.589 67	28.230 77	59	15.092 ± 0.002	13.964 ± 0.002	11.57 ± 0.05	5555	155 ± 7	09
GMP1853		195.445 90	28.095 00	87	14.877 ± 0.002	13.700 ± 0.002	11.20 ± 0.04	5836	190 ± 5	09
GMP2219		195.301 20	27.604 48	132	16.096 ± 0.003	14.979 ± 0.003	12.70 ± 0.08	7577	110 ± 3	09
GMP2584		195.148 22	28.146 12	169	15.502 ± 0.003	14.377 ± 0.003	11.97 ± 0.06	5437	136 ± 3	09
GMP2795	4895	195.074 70	28.202 40	154	13.864 ± 0.002	12.673 ± 0.002	10.14 ± 0.03	8513	201 ± 10	11
GMP2815	4894	195.068 83	27.967 51	32	15.478 ± 0.003	14.469 ± 0.003	11.88 ± 0.07	4664	85 ± 2	09
GMP2956		195.022 93	27.807 59	8	15.484 ± 0.003	14.360 ± 0.003	11.87 ± 0.05	6549	140 ± 10	11
GMP3423		194.872 53	27.850 16	154	15.249 ± 0.002	14.017 ± 0.002	11.50 ± 0.04	6895	213 ± 9	11
GMP3561	4865	194.832 83	28.084 30	115	14.367 ± 0.002	13.144 ± 0.002	10.48 ± 0.03	4651	203 ± 7	11
GMP3997		194.703 03	27.810 43	75	14.760 ± 0.002	13.575 ± 0.002	11.12 ± 0.04	5886	172 ± 10	11
GMP4664		194.447 10	27.833 31	90	15.600 ± 0.003	14.421 ± 0.003	12.03 ± 0.05	6046	155 ± 9	11
GMP4679		194.442 32	27.757 03	114	15.473 ± 0.003	14.412 ± 0.003	12.09 ± 0.07	6147	100 ± 13	11
GMP4907		194.357 67	27.546 13	142	15.401 ± 0.003	14.220 ± 0.002	11.84 ± 0.05	5638	145 ± 6	11
GMP5160		194.235 74	28.623 38	100	15.444 ± 0.003	14.300 ± 0.002	12.05 ± 0.06	6566	138 ± 3	09/11

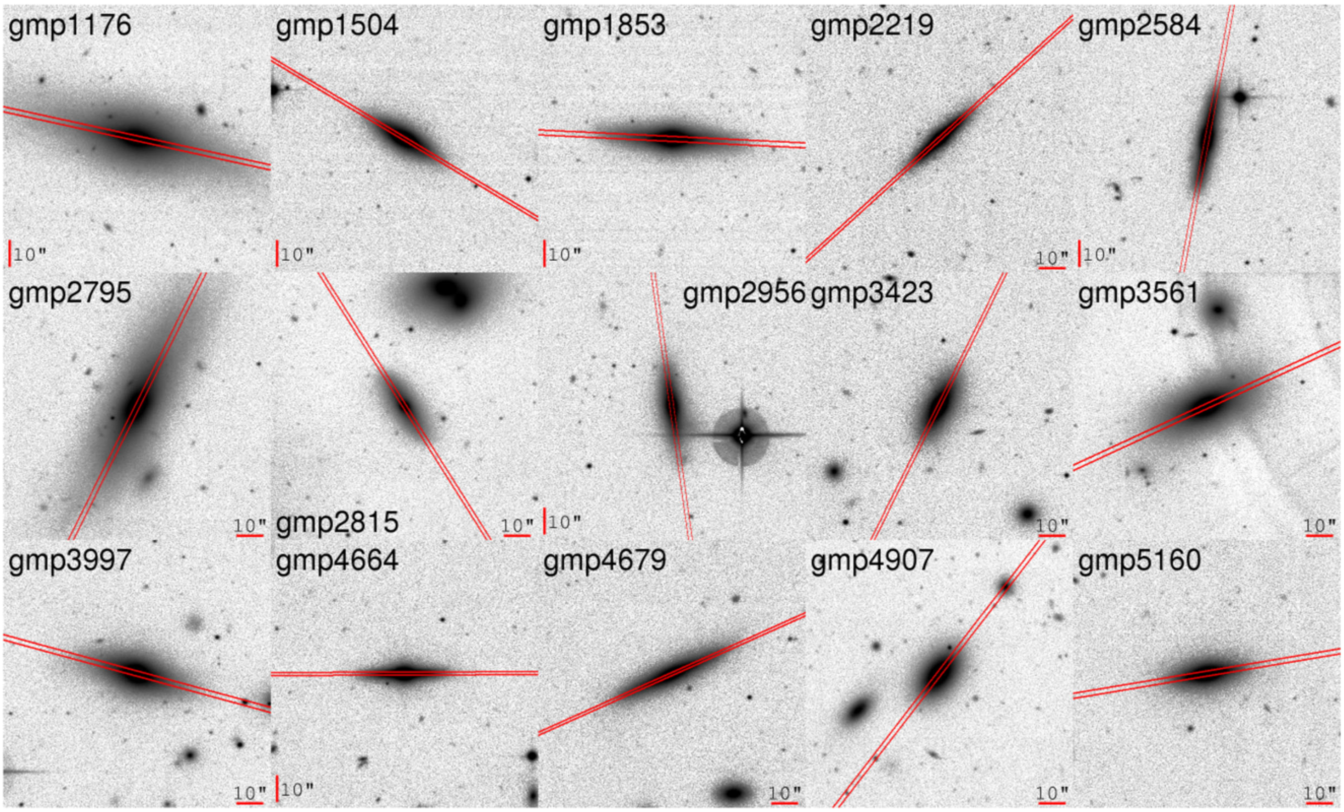

Figure 1. CFHT MegaCam g-band thumbnails (100 × 100 arcsec) for the GMOS S0 sample (north is up, east is left). The orientation of the major axis long slit is marked.

the slit was centred on the S0 bulge and orientated along the disc major axis, as shown in Fig. 1.

The galaxies were observed during dark time with the seeing <1.0 arcsec (FWHM) for all exposures, and better than 0.8 arcsec in many cases. In 2009, GMP5160 was observed in particularly cloudy conditions, and was re-observed in 2011, providing a convenient consistency check between the different instrument configurations of the two campaigns.

3 DATA REDUCTION AND ANALYSIS

3.1 Initial reduction

Initial data reduction uses the standard Gemini GMOS PYRAF routines. Variance frames are calculated from the quadrature sum of the Poisson noise in the raw detector counts and the read noise, and propagated through the same pipeline routines as the science

Table 2. GMOS instrument configuration.

	2009	2011
Mode	Long slit	
Grating	B1200	B600
Slit width	2 arcsec	1.5 arcsec
Slit length	330 arcsec	
CCD binning	4 × 4	
Wavelength range	4060–5522 Å	3600–6200 Å
Spectral resolution	5.1 Å FWHM ($\sigma \sim$136 km s^{-1})	8.5 Å FWHM ($\sigma \sim$226 km s^{-1})
Spectral sampling	∼0.95 Å pixel^{-1}	∼1.5 Å pixel^{-1}
Spatial sampling	0.2908 arcsec pixel^{-1}	

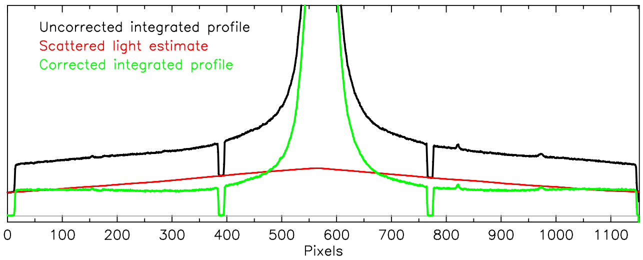

Figure 2. The integrated brightness profiles of the uncorrected (black) and scattered-light-corrected (green) frames for GMP1176. The red line shows the scattered light correction profile, as interpolated from the unexposed slit bridges and ends.

frames. We have assumed that the noise associated with bias and flat-field frames is negligible.

3.2 GMOS scattered light

Visual inspection of the raw detector frames shows that unexposed pixels in the slit bridges and beyond the slit ends do not have zero counts. The cause of this phenomenon is scattered light in the instrument, most likely due to the classically ruled grating (see Norris, Sharples & Kuntschner 2006), which is not accounted for in the standard reduction routines. The scattered light appears as a featureless constant offset which artificially enhances the continuum level, thus decreasing the measured absorption line strengths. The effect is increasingly significant as the galaxy surface brightness decreases (∼50 per cent of the measured flux in the outer regions of the galaxy), so scattered light tends to spuriously strengthen index gradients. For the kinematic analysis of this study, the scattered light correction is inconsequential, but we include it here for completeness.

To quantify the scattered light in each raw exposure, the flux is measured in the unexposed regions (slit bridges and ends). For each wavelength pixel, we interpolate between these regions (using two linear fits) to calculate the scattered light frame. For an example galaxy, Fig. 2 shows the interpolated scattered light along the spatial axis, in an arbitrary wavelength slice. The correction removes the inflated wings of the integrated surface brightness profile. During the reduction described above, the scattered light frame is subtracted from the raw image before wavelength calibration.

3.3 Bulge and disc decomposition

Structural parameters for each galaxy are determined from g-band CFHT MegaCam image data, with a point spread function FWHM of ∼0.7 arcsec and 3.4 times the depth of SDSS. An analytical Sérsic + exponential component model is fitted to thumbnail images using GALFIT (version 3.0.4; Peng et al. 2010). Initial values are generated from the best-fitting parameters of a Sérsic-only model. The search through chi-squared space was extended by perturbing parameters from their 'best-fitting' positions and refitting, thus improving reliability of the GALFIT-derived characteristics. Parameter uncertainties were estimated from the scatter in Monte Carlo fitting tests.

The Sérsic component corresponds to the bulge, parametrized by an effective radius $r_{\rm bul}$, Sérsic index n and ellipticity, $e_{\rm bul}$. The disc is modelled by the exponential component, parametrized by a scalelength $r_{\rm disc}$ and ellipticity, $e_{\rm disc}$. The disc inclination angle $i_{\rm disc}$ is calculated from the axis ratio via the standard formula

$$\cos i_{\rm disc} = \sqrt{\frac{(1-e_{\rm disc})^2 - q_0^2}{1-q_0^2}} \quad (1)$$

for which we assume an intrinsic axis ratio of $q_0 = 0.22$ (De Vaucouleurs et al. 1991). The derived bulge and disc parameters for all GMOS S0s are displayed in the top half of Table 3.

The luminosity profile of each component was computed numerically by integrating along a major axis slit in the best-fitting model image. The upper panels of Figs A1–A15 show the bulge,

Table 3. Bulge and disc parameters from the GALFIT decomposition described in Section 3.3. S0 galaxies from the GMOS sample are displayed in the top half of the table. Additional S0s from the Mehlert et al. (2000) and Hinz et al. (2003) samples (see Section 4.1) are shown below the dividing line, and were decomposed in exactly the same manner. The fits for GMP1614 and 3761 include an additional small bar component, as described in Section 4.1.

GMP ID	Sérsic bulge			Exponential disc		
	$r_{\rm bul}$ (arcsec)	n	$e_{\rm bul}$	$r_{\rm disc}$ (arcsec)	$e_{\rm disc}$	$i_{\rm disc}$ (deg)
GMP1176	13.1	6.1	0.58	3.1	0.94	∼90
GMP1504	1.6	4.3	0.22	3.9	0.71	79
GMP1853	2.3	3.0	0.37	7.1	0.82	∼90
GMP2219	9.2	3.9	0.58	4.2	0.88	∼90
GMP2584	2.5	4.7	0.13	5.7	0.85	∼90
GMP2795	3.5	1.4	0.38	12.3	0.72	80
GMP2815	0.8	1.4	0.16	4.4	0.66	75
GMP2956	4.0	3.4	0.50	5.0	0.82	∼90
GMP3423	3.5	5.4	0.46	3.5	0.78	89
GMP3561	2.5	1.5	0.43	7.6	0.58	69
GMP3997	2.3	2.2	0.26	7.0	0.67	75
GMP4664	1.4	2.3	0.30	4.7	0.85	∼90
GMP4679	32.3	9.8	0.22	7.2	0.85	∼90
GMP4907	2.0	3.8	0.39	3.2	0.48	61
GMP5160	11.4	10.0	0.25	3.8	0.78	89
GMP0756	5.6	3.1	0.55	12.3	0.75	82
GMP1111	4.2	4.3	0.40	4.8	0.87	∼90
GMP1223	5.6	3.0	0.48	6.0	0.57	67
GMP1614	1.7	1.7	0.22	6.5	0.27	45
GMP2413	1.5	1.8	0.17	6.5	0.47	61
GMP2431	4.8	4.6	0.21	8.9	0.48	61
GMP2535	4.2	2.8	0.46	6.3	0.36	52
GMP2629	2.3	2.9	0.42	7.1	0.46	60
GMP3273	1.7	1.3	0.08	8.8	0.72	80
GMP3367	1.1	2.1	0.13	4.3	0.29	46
GMP3414	1.0	1.6	0.15	5.0	0.41	56
GMP3661	1.1	1.9	0.29	5.8	0.29	47
GMP3761	4.9	4.5	0.04	6.1	0.63	72
GMP3818	3.1	2.9	0.30	5.7	0.65	74

disc and total luminosity profiles for each galaxy. Examining these best-fitting, two-component decompositions, the relative size of the bulges in this sample varies widely and can be separated into three broad categories. In most cases (12/15), the decomposed profile exhibits the 'classic' S0 form of a dominant bulge at small radii and a significant disc at large radii. In contrast, GMP1176 is better fitted by a dominant bulge at all radii, with a small embedded disc which only contributes a small fraction of the light even in the outskirts. The remaining two S0s (GMP3423, 4907) are an intermediate case, strongly resembling the 'classic' S0s, with a dominant bulge at small radii, but comparable contribution from bulge and disc components at large radii. The latter two categories may be better fitted by a three-component model including a large-scale spherical halo, although we do not attempt such a modelling in the current study.

3.4 Spatial binning and kinematic analysis

We use a simple adaptive-width algorithm in which the data are binned along the slit, imposing the criterion $\mathrm{S/N}_{\lambda=4700-5000} \gtrsim 20\,\mathrm{\AA}^{-1}$ as well as a minimum bin width of 0.5 arcsec. In the outermost bin, we simply use a width to maximize S/N.

The kinematic properties ($cz_{\rm hel}$, $V_{\rm obs}$, $\sigma_{\rm obs}$) are measured using the Penalized Pixel-Fitting (PPXF) IDL routine (Cappellari & Emsellem 2004). PPXF extracts kinematics by fitting to a large set of weighted stellar templates, virtually eliminating template mismatch. The non-linear least-squares direct pixel-fitting computation is broken into several iterations which find the best-fitting linear combination of the stellar templates. The derived residual spectrum from each iteration forms a penalization term in the non-linear optimization. The two central panels of Figs A1–A15 present the observed rotational velocity and velocity dispersion of each GMOS S0 galaxy. The penultimate column of Table 1 lists the observed maximum rotational velocity for each galaxy.

3.5 Derivation of circular velocities

We derive the maximum circular velocity from the observed velocity via the prescription described in Neistein et al. (1999), implemented in numerous S0 studies (e.g. Hinz et al. 2003; Bedregal et al. 2006b). For edge-on S0 galaxies (those with disc inclinations $i \gtrsim 60^\circ$), two steps are required to calculate the circular velocity at a given radius. First, we compute the kinematics in the azimuthal (ϕ) direction by accounting for line-of-sight integration through the disc. For an exponential disc with a scaleheight $h_s = 0.2 r_{\rm disc}$, Neistein et al. estimate corrections

$$V_\phi(r) = \frac{V_{\rm obs}(r)}{f(r/r_{\rm disc})} \quad (2)$$

$$\sigma_\phi(r)^2 = \sigma_{\rm obs}(r)^2 - \frac{1}{2}(V_\phi(r) - V_{\rm obs}(r))^2, \quad (3)$$

where

$$f(x) = \frac{\exp(-x)}{-0.5772 - \ln x + x - \frac{1}{2}x^2/2! + \frac{1}{3}x^3/3! - \cdots} - x, \quad (4)$$

and ($V_{\rm obs}$, $\sigma_{\rm obs}$) and (V_ϕ, σ_ϕ) are the observed and corrected azimuthal values, respectively. For inclinations $i > 70^\circ$, the error due to assuming $i = 90^\circ$ is $\Delta \log V_\phi \sim 0.025$. In most of the Coma S0 galaxies presented here, the observed velocity dispersion corresponding to the flat rotation curve region is less than half of the GMOS instrument resolution ($\sim$136 or 226 km s^{-1} for 2009/11, respectively), and we were unable to determine σ_ϕ.

The second stage corrects for 'asymmetric drift'. Although the net velocity of stars is zero in the vertical and radial directions, the average velocity in the azimuthal direction is not equal to the local circular velocity. The greater the random velocity for individual stars, the larger the lag between net motion and circular velocity. Neistein et al. (1999) correct for this effect using the formula

$$V_{\rm c}(r)^2 = V_\phi(r)^2 + \sigma_\phi(r)^2 \left(2\frac{r}{r_{\rm disc}} - 1\right). \quad (5)$$

The maximum circular velocity is calculated by taking the mean value of all $V_{\rm c}$ data points lying on the flat portion of the rotation curve (generally $1.5 < r/r_{\rm disc} < 2.5$). For the approximations in the asymmetric drift correction to hold, all points also have to conform to the constraint $V_\phi/\sigma_\phi > 2.5$. For the galaxies with no computed σ_ϕ, we were unable to correct for asymmetric drift and, when quoting $V_{\rm c}$ for these galaxies (final column of Table 6), we have given V_ϕ. However, as $V_{\rm c} \approx V_\phi$ if $\sigma_{\rm obs} \to 0$, this should not lead to a significant underestimation. To test this, we used the uncorrected $\sigma_{\rm obs}$ to account for the asymmetric drift (which overestimates the correction). The difference between this $V_{\rm c}$ and V_ϕ is $<$10 per cent of the uncertainty on the values, so will not have a significant effect on any conclusions.

For each galaxy in the Coma S0 sample, $V_{\rm c}$ is presented in Table 6. For GMP5160, we show the velocity derived from the 2011 data ($V_{\rm c} = 184 \pm 5$ km s^{-1}). From the 2009 observation, $V_{\rm c} = 170 \pm 13$ km s^{-1}, as poor S/N severely limits the radial extent of the data.

3.6 Absolute magnitude derivation

Absolute magnitudes are calculated in each band ($X = g$, i, $K_{\rm s}$) using

$$M_X = m_X - A_{i,X} - A_{g,X} - A_{k,X} - \mu_{\rm Coma}, \quad (6)$$

where the internal extinction $A_{i,X} = \gamma_X \log(a/b)$; Galactic extinction $A_{g,X}$ and k-correction $A_{k,X}$ are derived in each band from the values listed in Table 4. The axis ratio is estimated via

$$\log(a/b) = \frac{1}{\sqrt{0.96 i_{\rm disc}^2 + 0.04}}. \quad (7)$$

For the S0 sample, we can assume that the internal extinction for S0s is zero, i.e. $\gamma_X = 0$. Cluster S0 galaxies, including those in the Coma sample (see Section 5.2.1), are observed to form a tight red sequence in optical colours, with less than 0.02 mag of the scatter unaccounted for by stellar population differences (Smith, Lucey & Hudson 2009). Such homogeneity is unlikely to occur unless the internal extinction is very small in all S0s. Indeed, dusty early-type galaxies are generally rare in clusters (Kaviraj et al. 2012) and only two of our S0 sample have even a hint of a dust lane (GMP3273, 3818). The Herschel Reference Survey has recently shown that local S0s are $\sim$10–100 times less dusty than spirals (Smith et al. 2012c). As spiral galaxies in the Coma cluster require a mean extinction correction of only $\sim$0.3 mag in the g band and $\sim$0.1 mag in $K_{\rm s}$ (Section 4.2), the internal extinction correction for S0 galaxies is likely to be very small. We note many other recent studies also assume a zero internal extinction for S0s (e.g. Bedregal et al. 2006b; Davis et al. 2011).

We adopt the distance modulus $\mu_{\rm Coma} = 35.05$ mag from NED (Virgo+NED velocity field model). Due to thisassumption of an equal line-of-sight depth for all galaxies, the error on the magnitude, δM_X, includes an additional 0.03 mag uncertainty for S0s, added in quadrature with the measurement error δm_X.

Table 4. Parameters used to derive the absolute magnitude in each band. V_c is the circular velocity, $\log(a/b)$ is the axial ratio, $E(B-V)$ is the extinction coefficient and z is the redshift. Note that the internal extinction correction, parametrized by γ_X, is different for the S0 and spiral samples.

	g		i		K_s	
γ_X (S0s)	0.0		0.0		0.0	
γ_X (spirals)	$1.51 + 2.46(\log(V_c) - 2.5)$	(1)	$1.00 + 1.71(\log(V_c) - 2.5)$	(1)	$\log(a/b) > 0.5$: $1.1 + 0.13/\log(a/b)$ $\log(a/b) < 0.5$: 0.26	(4)
$A_{g,X}$	$3.793 \times E(B-V)$	(2)	$2.086 \times E(B-V)$	(2)	$0.367 \times E(B-V)$	(4)
$A_{k,X}$	0.01	(3)	0.00	(3)	$1.52z$	(4)

(1) Hall et al. (2012), (2) Schlegel, Finkbeiner & Davis (1998), (3) Blanton & Roweis (2007), (4) Masters, Giovanelli & Haynes (2003).

4 ADDITIONAL COMA SAMPLES

4.1 Extended Coma S0 sample

We supplement our GMOS Coma S0 sample with data from two previous studies, Mehlert et al. (2000, hereafter M00) and Hinz et al. (2003, hereafter H03). For each additional S0, SDSS and 2MASS total magnitudes are obtained from the catalogues described above. GMP3414 does not have a counterpart in the K_s band.

Although these galaxies are all typed S0 by M00 and H03, four are not strictly classified S0 according to D80: GMP1614 = SB0, GMP2431 = Sa, GMP3761 = SB0, GMP3818 = S0/a. Four further galaxies are not included in D80, while the NED 'homogenized' classification gives GMP0756 = S0, GMP1111 = S0, GMP1900 = Sab, GMP3273 = S0/a. Visual inspection of the MegaCam imaging (displayed in Fig. 3) agrees with these types. GMP1900 (from H03) is clearly a spiral with clumpy structure in the disc, and is removed from our S0 sample. We concur with the NED classification of GMP2431, which appears closer in morphology to an S0/a than the D80 Sa type, exhibiting very little structure and only incredibly weak arms. We retain the three S0/a galaxies (GMP2431, 3273, 3818) in the S0 sample.

The bulge/disc decomposition parameters are derived from MegaCam optical imaging using the method described in Section 3.3, and are displayed below the GMOS sample in Table 3. As with the GMOS S0s, the majority (12/14) exhibit the 'classic' S0 structure. GMP2535 has an equal bulge and disc contributions at large radii, while GMP1614 is bulge dominated throughout. As GMP1614 is typed as SB0 by D80, we attempt to fit an additional bar component, finding that the profile is best fitted by a 'classic+bar' solution, with the bulge dominating in the centre and the disc at large radii. The bar is subdominant at all radii, but contributes enough flux to remove the extended bulge. We note that although

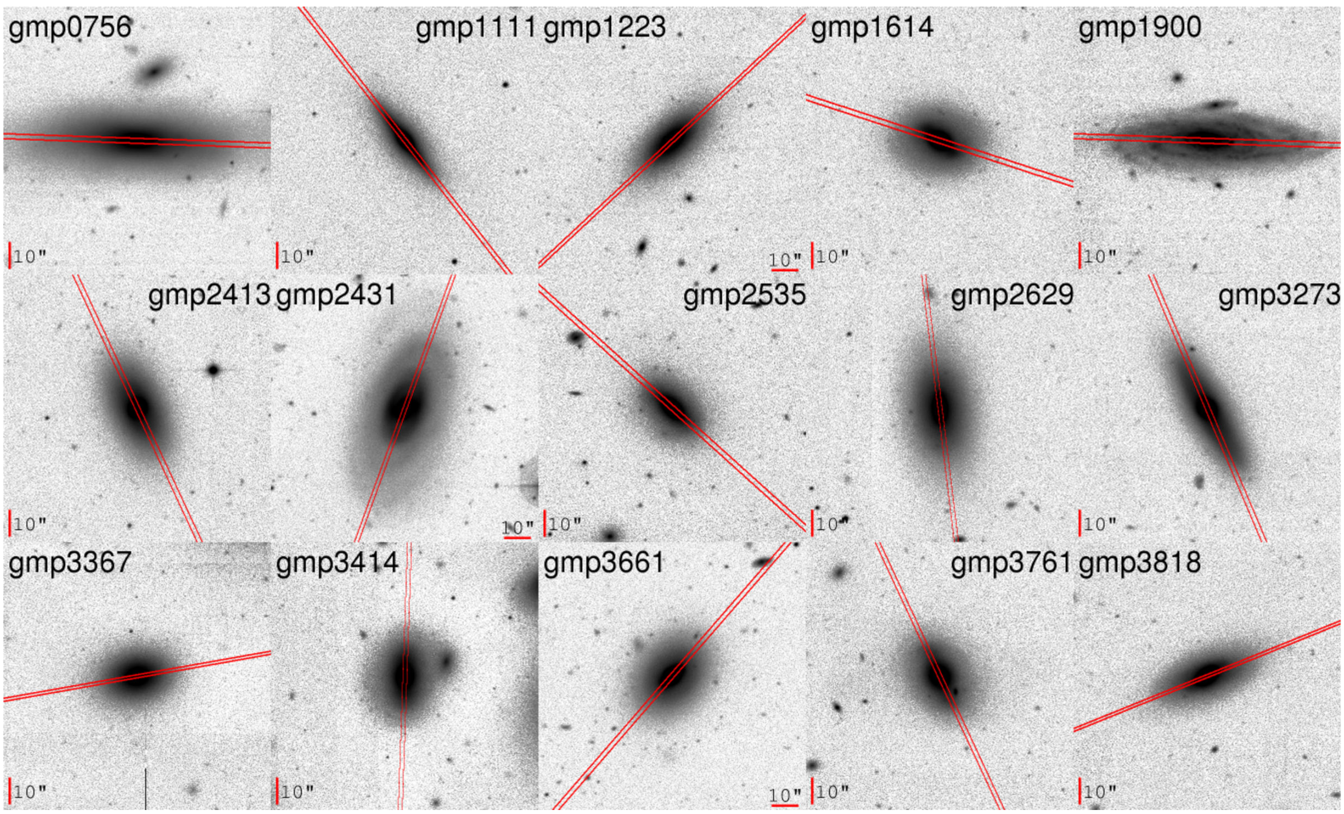

Figure 3. CFHT MegaCam g-band thumbnails (100 × 100 arcsec) for the additional 14 S0 galaxies (north is up, east is left) and GMP1900 which is thrown out of the S0 sample with an obviously spiral-like disc. The orientation of the major axis long slit is marked.

Table 5. Additional Coma cluster S0 galaxies from M00 and H03. ID, position and photometric parameters as in Table 1. For M00, cz and $V_{\rm obs}$ are measured using the same method as for the GMOS sample. For the H03 sample, raw spectra are unavailable so cz and $V_{\rm c}$ are taken directly from the paper (see Section 4.1.2).

GMP ID	NGC #	RA (J2000)	Dec. (J2000)	PA (deg)	m_g (mag)	m_i (mag)	$m_{K_{\rm s}}$ (mag)	$cz_{\rm hel}$ (km s^{-1})	$V_{\rm obs}$ (km s^{-1})	
GMP0756	4944	195.958 12	28.185 73	88	13.436 ± 0.002	12.349 ± 0.002	10.00 ± 0.03	6989	206 ± 10	M00
GMP1111		195.790 57	28.583 52	38	14.985 ± 0.002	13.821 ± 0.002	11.38 ± 0.04	6922	–	H03
GMP1223		195.735 72	28.070 39	133	15.348 ± 0.003	14.282 ± 0.002	12.13 ± 0.09	7759	–	H03
GMP1614		195.536 08	28.387 11	72	14.896 ± 0.002	13.650 ± 0.002	11.13 ± 0.05	7605	–	H03
GMP2413		195.217 01	28.366 13	25	14.408 ± 0.002	13.255 ± 0.002	10.82 ± 0.03	7665	197 ± 25	M00
GMP2431		195.208 01	27.405 78	160	14.603 ± 0.002	13.572 ± 0.002	11.45 ± 0.06	6569	–	H03
GMP2535		195.170 20	27.996 60	48	15.211 ± 0.002	14.043 ± 0.002	11.66 ± 0.06	7112	90 ± 16	M00
GMP2629	4896	195.128 20	28.346 36	7	14.353 ± 0.002	13.196 ± 0.002	10.76 ± 0.03	6012	177 ± 28	M00
GMP3273		194.913 00	28.895 52	23	14.508 ± 0.002	13.212 ± 0.002	10.51 ± 0.03	6210	–	H03
GMP3367	4873	194.886 63	27.983 60	100	14.804 ± 0.002	13.585 ± 0.002	11.25 ± 0.04	5818	–	H03
GMP3414	4871	194.874 84	27.956 43	178	14.758 ± 0.002	13.522 ± 0.002	–	6729	115 ± 27	M00
GMP3661		194.807 10	27.402 57	139	15.173 ± 0.002	14.009 ± 0.002	11.44 ± 0.05	5675	126 ± 24	M00
GMP3761		194.775 09	27.996 70	25	14.985 ± 0.002	13.724 ± 0.002	11.38 ± 0.05	7678	–	H03
GMP3818		194.757 54	28.225 36	112	14.820 ± 0.002	13.610 ± 0.002	11.04 ± 0.04	8017	–	H03

the addition of a bar component significantly reduces the measured effective radius of the bulge (>4 times smaller), the disc scalelength is more stable (<50 per cent decrease), and the corrected circular velocity remains virtually unchanged.

The disc inclination, displayed in the final column of Table 3, shows that the M00 and H03 S0s are generally not as edge-on as the GMOS sample. Observed parameters for the M00 (six unique S0s) and H03 (eight unique S0s) samples are shown in Table 5. The following two subsections describe differences between the derivation of the Tully–Fisher (TF) parameters for S0s in the M00, H03 and our GMOS sample. The final TF parameters for the full S0 sample (29 Coma S0s) are presented in Table 6.

4.1.1 S0s from M00

M00 obtained long-slit spectra for a sample of 13 Coma S0s using spectrographs on the 2.5–3.5 m-class telescopes of the Michigan-Dartmouth-MIT, McDonald and German-Spanish (at Calar Alto) observatories. Five of these galaxies are also in the GMOS sample (GMP1176, 1853, 2795, 3561, 4679).

We use the spatially binned observed kinematic properties ($V_{\rm obs}$, $\sigma_{\rm obs}$), provided by the authors in an appendix to their original paper, and recalculate $V_{\rm c}$ using exactly the same method as described in Section 3.5. For two S0s (GMP3073, 5568), S/N beyond the central bin is too low and the galaxies are removed from our sample. GMP2535 and GMP3414 are also faint and while the spectroscopy does probe disc-dominated radii, the data may not extend quite far enough to fully constrain the maximum rotational velocity. We retain these two S0s in our sample, but keep this concern in mind.

For the galaxies overlapping with the GMOS sample, we can assess the quality of the M00 data directly and also recalculate $V_{\rm c}$ from their observations using our method. Generally, our GMOS data probe further into the disc-dominated regime, by as much as twice the observed radius in two cases. This leads to a two to three times increase in usable velocity data points in the disc and hence smaller uncertainties. For the five galaxies in common, the mean difference in $V_{\rm c}$ is only 7 km s^{-1} (GMP1176: 192 and 187 km s^{-1} for the GMOS and M00 data, respectively; GMP1853: 190 and 174; GMP2795: 201 and 197; GMP3561: 203 and 201; GMP4679: 100 and 92). These offsets are less than the typical measurement uncertainty of ∼14 km s^{-1}.

4.1.2 S0s from H03

H03 observed a sample of 15 Coma cluster S0s using the blue channel long-slit spectrograph on the 6.5 m MMT. With the raw spectra for these observations inaccessible on tape (Hinz, private communication), we use the values of $V_{\rm c}$ presented in the original paper. We note that H03 obtain the circular velocity via the same methodology with the same corrections as presented in Section 3.5. From H03 (fig. 4), we see that four of the spectra do not reach the required S/N beyond the central bin (GMP2413, 2495, 4664, 4907) and these S0s are cut from our sample. We also note that while the data for GMP1223 probe the disc-dominated regime, the maximal velocity may not be fully constrained: we retain this S0, but remember this potential shortcoming. Two of the remaining galaxies overlap with the GMOS sample (GMP3423, 3997). Finally, as we noted previously, GMP1900 is a spiral galaxy and is not included in our S0 sample.

The two galaxies with adequate data from both GMOS and H03 offer a useful indicator of the compatibility of the derived velocities from the two studies. H03 present $V_{\rm c} = 317 \pm 31$ km s^{-1} for GMP3423 and $V_{\rm c} = 267 \pm 19$ km s^{-1} for GMP3997. These maximum velocities are well within the errors of our GMOS values, $V_{\rm c} = 306 \pm 25$ and 265 ± 15 km s^{-1}, respectively, giving us confidence in using the remaining H03 velocity measurements to increase our sample size.

4.2 Coma cluster spiral sample

We wish to compare the S0 population to spiral galaxies in the Coma cluster. The SFI++ TF catalogue (Springob et al 2007) contains H I line widths log(W) and disc inclinations $i_{\rm disc}$ for a sample of nearly 5000 spiral galaxies in the local Universe. This includes 38 Coma cluster members (including GMP1900 from H03), which form our spiral sample. For each of the Coma spiral galaxy, g-, i- and $K_{\rm s}$-band total apparent magnitudes are extracted from SDSS and 2MASS in the same manner as for the S0s. Two faint spirals do not have $K_{\rm s}$-band counterparts in the 2MASS XSC. The observed properties for the spiral sample are presented in Table B1.

Derivation of the TF parameters ($V_{\rm c}$, M_X) for the spiral sample differs in two key respects compared to the S0 analysis: the measurement of the rotational velocities and the internal extinction correction.

Table 6. Final TF parameters for all 29 Coma cluster S0 galaxies in the GMOS, M00 and H03 samples. Δd_{CC} is the projected cluster-centric distance from the nominal cluster centre (RA = 194.9660, Dec. = 27.968 49), and Σ is the density parameter described in Section 4.3. $E(B-V)$, g- and i-band photometry from SDSS (AB mags); K_s band from 2MASS (Vega mags). Absolute magnitude in each band M_X are corrected for Galactic extinction, internal extinction and k-correction as described in Section 3.6. δM_X includes 0.03 mag uncertainty from the assumption that every galaxy is at the same line-of-sight depth (the cluster mean). Maximum circular velocity (V_c km s^{-1}) as derived in Sections 3.5, 4.1.1 and 4.1.2 (GMOS, M00 and H03, respectively).

GMP ID		Δd_{CC} (Mpc)	Σ (Mpc^{-2})	$E(B-V)$	M_g (mag)	M_i (mag)	M_{K_s} (mag)	V_c (km s^{-1})
GMP0756	M00	1.49	52	0.008	−21.65 ± 0.03	−22.72 ± 0.03	−25.09 ± 0.15	314 ± 19
GMP1111	H03	1.57	32	0.009	−20.11 ± 0.03	−21.25 ± 0.03	−23.71 ± 0.15	208 ± 12
GMP1176	09	1.16	49	0.011	−21.30 ± 0.03	−22.40 ± 0.03	−24.77 ± 0.15	266 ± 12
GMP1223	H03	1.14	55	0.009	−19.75 ± 0.03	−20.79 ± 0.03	−22.97 ± 0.17	107 ± 9
GMP1504	09	1.01	67	0.009	−20.00 ± 0.03	−21.11 ± 0.03	−23.51 ± 0.16	204 ± 8
GMP1614	H03	1.08	31	0.009	−20.20 ± 0.03	−21.42 ± 0.03	−23.96 ± 0.16	256 ± 50
GMP1853	09	0.73	53	0.008	−20.21 ± 0.03	−21.37 ± 0.03	−23.88 ± 0.15	279 ± 11
GMP2219	09	0.78	29	0.008	−18.99 ± 0.03	−20.09 ± 0.03	−22.40 ± 0.17	152 ± 6
GMP2413	M00	0.75	53	0.010	−20.69 ± 0.03	−21.81 ± 0.03	−24.27 ± 0.15	294 ± 24
GMP2431	H03	1.00	17	0.008	−20.49 ± 0.03	−21.50 ± 0.03	−23.64 ± 0.16	177 ± 58
GMP2535	M00	0.30	196	0.011	−19.89 ± 0.03	−21.03 ± 0.03	−23.42 ± 0.16	136 ± 20
GMP2584	09	0.40	76	0.012	−19.60 ± 0.03	−20.70 ± 0.03	−23.11 ± 0.16	185 ± 4
GMP2629	M00	0.67	55	0.010	−20.75 ± 0.03	−21.88 ± 0.03	−24.32 ± 0.15	259 ± 33
GMP2795	11	0.42	103	0.012	−21.24 ± 0.03	−22.40 ± 0.03	−24.95 ± 0.15	318 ± 21
GMP2815	09	0.15	377	0.010	−19.62 ± 0.03	−20.60 ± 0.03	−23.19 ± 0.17	121 ± 7
GMP2956	11	0.28	261	0.008	−19.61 ± 0.03	−20.71 ± 0.03	−23.22 ± 0.16	199 ± 16
GMP3273	H03	1.54	13	0.011	−20.59 ± 0.03	−21.86 ± 0.03	−24.58 ± 0.15	269 ± 8
GMP3367	H03	0.12	622	0.009	−20.29 ± 0.03	−21.48 ± 0.03	−23.83 ± 0.16	375 ± 50
GMP3414	M00	0.13	796	0.010	−20.34 ± 0.03	−21.55 ± 0.03	–	171 ± 27
GMP3423	11	0.24	378	0.011	−19.85 ± 0.03	−21.06 ± 0.03	−23.59 ± 0.15	307 ± 25
GMP3561	11	0.27	159	0.010	−20.73 ± 0.03	−21.93 ± 0.03	−24.59 ± 0.15	308 ± 17
GMP3661	M00	0.97	21	0.008	−19.92 ± 0.03	−21.06 ± 0.03	−23.64 ± 0.16	189 ± 25
GMP3761	H03	0.28	264	0.011	−20.12 ± 0.03	−21.35 ± 0.03	−23.71 ± 0.16	267 ± 40
GMP3818	H03	0.52	53	0.011	−20.28 ± 0.03	−21.46 ± 0.03	−24.05 ± 0.15	234 ± 22
GMP3997	11	0.47	492	0.013	−20.35 ± 0.03	−21.50 ± 0.03	−23.97 ± 0.16	265 ± 15
GMP4664	11	0.79	131	0.011	−19.50 ± 0.03	−20.65 ± 0.03	−23.06 ± 0.16	215 ± 10
GMP4679	11	0.84	72	0.011	−19.63 ± 0.03	−20.66 ± 0.03	−22.99 ± 0.16	148 ± 12
GMP4907	11	1.13	116	0.009	−19.69 ± 0.03	−20.85 ± 0.03	−23.24 ± 0.16	212 ± 12
GMP5160	11	1.52	12	0.011	−19.66 ± 0.03	−20.77 ± 0.03	−23.04 ± 0.16	184 ± 5

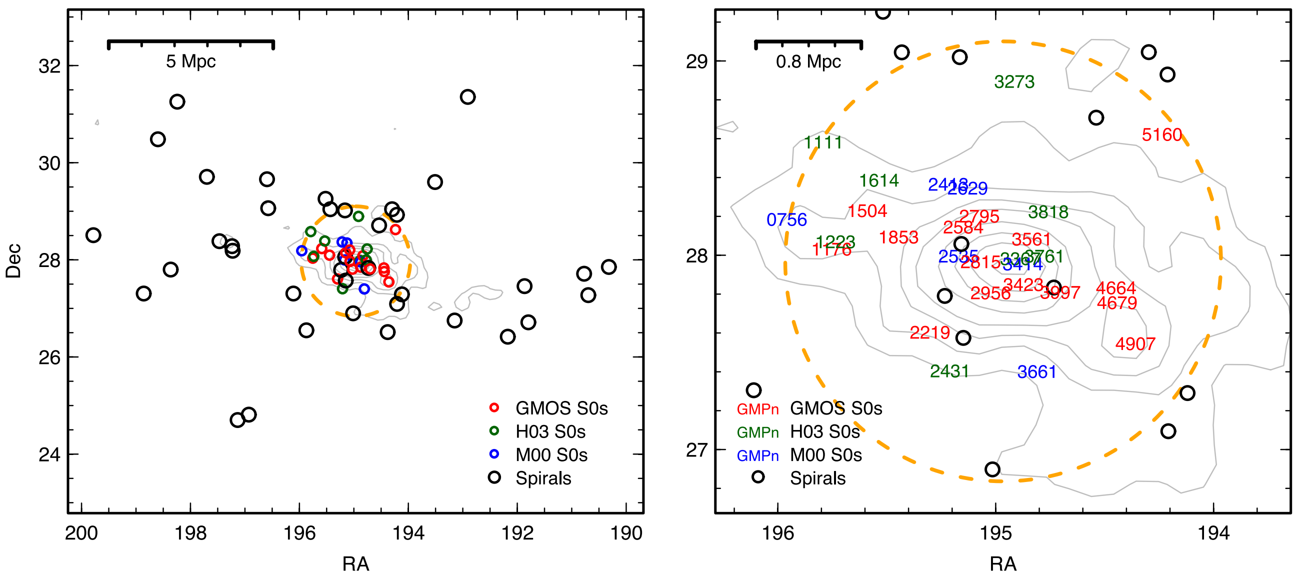

Figure 4. Spatial distribution of the S0 (red = GMOS, blue = M00, green = H03) and spiral (black) samples within the Coma cluster. The spiral sample extends to significantly larger radii so two levels of zoom are shown: in both panels the thick dashed orange circle shows a projected cluster-centric radius of 1° (1.66 mpc at the distance of the Coma cluster). The grey contours represent the local galaxy density, as derived from the SDSS sample described in Section 4.3.

For the spirals, rotational velocity is usually derived from H I line widths, measured at 50 per cent of the total flux and corrected for instrument effects. For the Coma spirals, we adopt the widths from Springob et al (2007) and assume that the maximum rotational velocity is half of the inclination-corrected line width; this does not attempt to account for turbulent motion intrinsic to the H I gas.

Several spirals in the full SFI++ catalogue have both H I line width measurements and Hα long-slit gas kinematic rotation curves, allowing a direct comparison of V_c derived from the two methods. Catinella, Haynes & Giovanelli (2007) show that the mean difference $V_{c,\rm H\,I} - V_{c,\rm H\alpha} = +24 \pm 4\,\rm km\,s^{-1}$, with a systematic dependence on the surface brightness profile (larger differences are associated with brighter bulges). A similar mean difference has also been reported by other authors (Courteau 1997; Raychaudhury et al. 1997). While the usually adopted technique to determine V_c from Hα rotation curve data (see e.g. Courteau 1997) is not precisely the same as the method we have used for our S0 absorption line rotation curves (Section 3.5), these techniques for near-edge-on disc galaxies are practically identical.

Correction of the H I-derived V_c to the optical rotation curve system would move the spiral TFR systematically towards marginally lower velocities (~0.03 dex) and flatten the relation in log space. Pre-empting the discussion in Section 5.1, we note that our Coma spiral TFR (uncorrected for the above offset) compares well to the TFR reported by Pizagno et al. (2007), who also derive V_c from Hα rotation curves. Pizagno et al. also use a different functional form for the rotation curve; (their equation 1). Refitting the GMOS S0s with this alternative function, we derive V_c with a mean offset of $1 \pm 9\,\rm km\,s^{-1}$, which is comparable to the uncertainty. Generally for edge-on disc galaxies, different methods of calculated V_c only result in marginal differences and for simplicity we choose not to apply an additional correction to the spiral V_c measurements.

The other significant difference between spiral and S0 TF parameters is the internal extinction correction. Whereas we assume that S0s lack significant internal extinction (Section 3.6), the dusty spirals require an inclination-dependent correction. In the SDSS bands, we use the corrections from Hall et al. (2012), which are based on the observed optical internal extinction of spiral galaxies reported by Tully et al. (1998). In the K_s band, we apply the empirical corrections from Masters et al. (2003), which are considered the standard for extragalactic infrared photometry (e.g. Masters, Springob & Huchra 2008; Jarrett et al. 2013). The exact form of these corrections is given in Table 4. The mean internal extinction correction for the spiral sample is 0.34 ± 0.10, 0.22 ± 0.07 and 0.10 ± 0.02 mag in the g, i and K_s bands, respectively.

Photometric corrections for the spirals (including internal extinction) are applied as described by equation (6). We use the Coma cluster distance modulus as for the S0s, but adopt an error of 0.12 to allow for the broader line-of-sight distribution of the spirals (cf. 0.03 mag adopted for the S0s; Section 3.6).

The derived TF parameters for the Coma cluster spiral sample are presented in Table B2 (cf. Table 6 for the S0 equivalent).

4.3 Local density and the full SDSS Coma sample

Fig. 4 displays the position of our Coma S0 and spiral samples on the sky. We aim to examine the environmental dependence of the S0 TFR. The simplest approach is to use the projected cluster-centric radius as an indicator of local density, effectively assuming spherical symmetry in the Coma cluster. Line-of-sight distance and differential velocity with respect to the total system are degenerate, so we do not attempt to correct for projection. However, we note that the effect can only decrease the apparent radius (increase apparent local density) as outer members are projected on to inner regions.

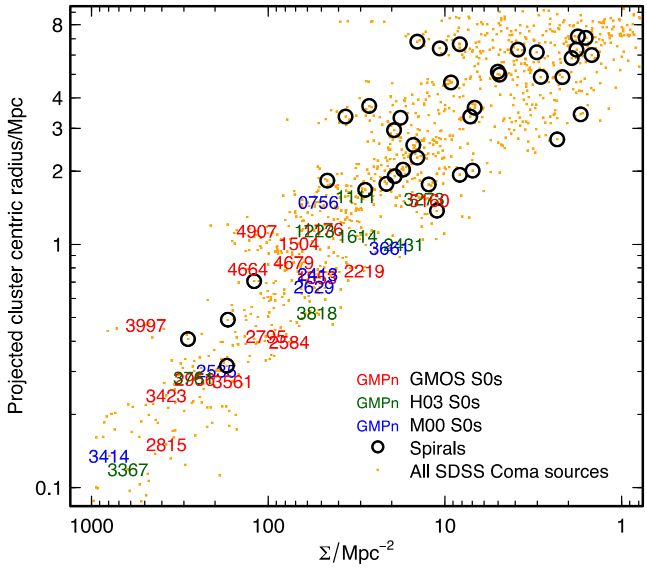

Figure 5. Comparison of the projected cluster-centric radius and the projected local galaxy density parameter Σ, as defined in Section 4.3. The full SDSS spectroscopic cluster member sample is shown by orange dots; other symbols as in Fig. 4. The deviations from linearity indicate regions where the galaxy distribution departs from a projected circular symmetry.

We account for the non-spherical morphology of the cluster by deriving the local density for each galaxy via a nearest-neighbour algorithm. Such a density parameter requires a complete selection of galaxies within the Coma cluster. We select all sources in the SDSS DR9 specphot catalogue[4] (the intersection of the full primary science spectroscopic and photometric catalogues) within $\pm 3500\,\rm km\,s^{-1}$ of the Coma cluster systemic redshift ($z = 0.0231$) and with an r-band magnitude M_r < -18 mag. There are 1113 such galaxies within a 5° radius of the nominal cluster centre.

We adopt the density parameter, Σ, from Baldy et al. (2006), which is defined as follows:

$$\Sigma = \frac{1}{2}\left[\frac{4}{\pi d_4^2} + \frac{5}{\pi d_5^2}\right], \qquad (8)$$

where d_N is the projected comoving distance to the Nth nearest cluster member. We calculate Σ for each galaxy, and display the local density as contours in Fig. 4. Fig. 5 compares this Σ parameter to the projected cluster-centric radius. The generally good correspondence suggests that the Coma cluster is mostly relaxed, although some significant substructure is revealed, such as the south-west overdensity, indicated by a bulge to larger Σ at ~1 Mpc.

5 RESULTS AND DISCUSSION

5.1 S0 TFR

The TFR links the luminosity of spirals to their maximum circular velocity. If S0s are quenched spirals, the ageing stellar population would result in a luminosity decrease. In contrast, the galaxy mass (and hence rotational velocity) should remain constant causing an offset between the spiral and S0 TFRs.

[4] accessed via http://skyserver.sdss3.org/CasJobs/

Table 7. The Coma cluster S0 TF offset in the g, i and K_s bands (Column 6). Columns 2–5 describe the reference spiral TFR in the form $M_X = a(\log V_c - \log V_0) + b$, where $\log V_0 = 2.220$, and σ_{Sp} is the dispersion in the magnitude axis. In each case, the gradient of the Coma cluster S0 TFR (fitted to our S0 sample) is fixed to the reference spiral relation. The S0 offset and dispersion σ_{S0} are given in the direction of luminosity. Note that Tully & Courtois (2012) report I_C-band results; for Coma spirals $m_i = m_{I_C} + 0.43$.

Band	Reference spiral TFR	a	b	σ_{Sp} (mag)	Coma S0 offset (mag)	σ_{S0} (mag)
	Pizagno et al. (2007)	− 5.48 ± 0.23	− 20.69 ± 0.04	0.45	**1.17 ± 0.15**	**0.58**
g	Hall et al. (2012)	− 8.04 ± 0.26	− 20.54 ± 0.05	0.26	**1.32 ± 0.12**	**0.84**
	Coma cluster (this Study)	**− 6.17 ± 0.45**	**− 20.54 ± 0.04**	**0.31**	**1.10 ± 0.18**	**0.64**
	Pizagno et al. (2007)	− 6.32 ± 0.22	− 21.39 ± 0.04	0.42	**0.83 ± 0.14**	**0.58**
	Hall et al. (2012)	− 8.71 ± 0.24	− 21.50 ± 0.05	0.26	**1.23 ± 0.12**	**0.87**
i	Tully & Courtois (2012)	− 8.81 ± 0.16	− 21.15 ± 0.04	0.41	**1.03 ± 0.14**	**0.88**
	Tully & Courtois (2012) [Coma only]	− 6.96 ± 0.56	− 21.42 ± 0.06	0.27	**0.94 ± 0.12**	**0.68**
	Coma cluster (this Study)	**− 7.04 ± 0.45**	**− 21.33 ± 0.05**	**0.32**	**0.86 ± 0.19**	**0.69**
	Masters et al. (2008)	− 7.25 ± 0.11	− 23.63 ± 0.08	0.40	**0.80 ± 0.12**	**0.55**
K_s	Williams, Bureau & Cappellari (2010)	− 8.15 ± 0.76	− 23.06 ± 0.11	0.37	**0.35 ± 0.11**	**0.54**
	Coma cluster (this Study)	**− 7.31 ± 0.49**	**− 23.66 ± 0.07**	**0.35**	**0.83 ± 0.19**	**0.67**

We consider the TFR in the g, i and K_s bands. In each band, we derive the best-fitting spiral TFR via an orthogonal regression, using the uncertainty in both parameters, as the least biased numerical fitting method available (Hall et al. 2012, and references therein). The S0 TFR is then calculated using the spiral TFR gradient as a reference. The best-fitting parameters for all the TFRs described in this section are given in Table 7.

5.1.1 g-band TFR

The g-band TFR for the 38 spirals in our Coma cluster sample (Table B2) is shown in Fig. 6. The best-fitting relation is $M_g \propto (-6.17 \pm 0.45) \log V_c$, with an rms dispersion of 0.31 mag.

We verify the reliability of this TFR by comparing to previous studies of larger samples. Recently, Hall et al. (2012) presented local spiral TFRs using newly derived photometry from DR7 SDSS images. For a 'best' sample of 668 spirals, they derive rotational velocities from H I line widths in the Springob et al (2007) SFI++ catalogue, using exactly the same method as for our spiral sample (Section 4.2). Using the same orthogonal fitting method, they report a steeper gradient of −8.04 ± 0.26. Several of our Coma spirals are included in the Hall et al. sample, and we find no significant difference in the TF parameters of these individual galaxies (rms dispersion of $\Delta V_c < 1\,\mathrm{km\,s^{-1}}$). In their section 7.1, Hall et al. suggest that their steep gradient results from a lack of explicit morphological selection: the sample includes a large fraction of early-type spirals (including many S0/a galaxies), particularly at higher luminosity, compared to other studies. In contrast, less than one quarter of our Coma cluster spiral sample is listed as Sa or Sab by NED, and of course includes no S0 or S0/a galaxies.

Pizagno et al. (2007) present a sample of 200 local spirals with no morphological selection. Photometry is taken from SDSS, while maximum rotational velocity is derived from Hα rotation curves, using a long-slit kinematic analysis similar to the method we describe for our S0s in Section 3.5. Pizagno et al. use a bivariate fit to their data, deriving a gradient of −5.48 ± 0.23 and an rms dispersion of 0.45 mag. The marginally shallower gradient can be attributed to the fitting method (Hall et al. 2012), and the TFR is compatible with our Coma relation, despite the very different origin of the V_c measurement.

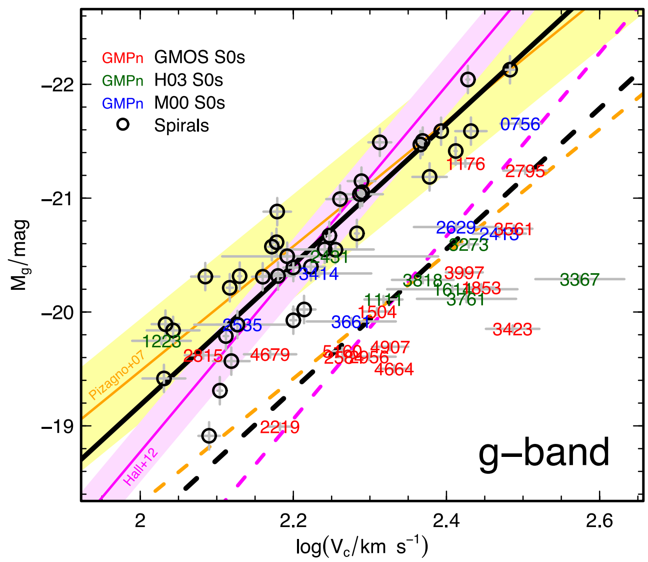

Figure 6. The g-band TFR for the Coma cluster. S0s are represented by their GMP ID number, while spirals are shown as black circles. The black solid line shows the best orthogonal regression fit to the Coma spiral TFR (gradient = −6.17 ± 0.45), while the black dashed line shows the best fit to the S0 sample, fixing the gradient to match the Coma spirals. The mean S0 offset is 1.10 ± 0.18 mag. Additional spiral TFRs are shown by the orange (Pizagno et al. 2007, gradient = −5.48 ± 0.23) and magenta (Hall et al. 2012, gradient = −8.04 ± 0.26) solid lines (yellow and purple shaded regions correspond to 1σ dispersions). Best-fitting Coma S0 TFRs fixed to these spiral reference gradients are shown by orange and magenta dashed lines.

We now consider the Coma cluster S0 sample comprising 29 galaxies (Table 6). The S0s are significantly offset from the Coma spiral relation. Assuming the same gradient as the spiral TFR, we calculate the mean S0 offset from the spirals to be 1.10 ± 0.18 mag. At a given rotational velocity, S0s in the Coma cluster are on average fainter than spirals by more than a magnitude. The mean offset is more than three times the rms dispersion of the spirals. For comparison, we also calculate the S0 offset assuming the spiral TFR from the two studies discussed above: 1.32 ± 0.12 and 1.17 ± 0.15 mag from the Hall et al. and Pizagno et al. TFRs, respectively

(Table 7). The larger offset from the Hall et al. TFR is a consequence of the steeper gradient.

A few individual galaxies in our analysis warrant further comment, starting with the five M00/H03 objects not strictly classified as S0 (see Section 4.1). The two SB0 (GMP1614, 3761) and two S0/a (GMP3273, 3818) exhibit an offset indistinguishable from the true S0s. In contrast, GMP2431 (designated Sa by D80, but S0/a in NED) is located close to the spiral TFR. Several other S0s have small offsets from the spiral TFR, and most were previously identified as having possibly underestimated maximum velocities due to shallow spectroscopy (GMP1223, 2535, 3414; Sections 4.1.1 and 4.1.2). For these to be located on the mean S0 relation, V_c would need to be larger by 40–70 km s^{-1}, which is not implausible given the shape of their observed velocity curves. However, the GMOS S0s with the smallest TFR offsets (GMP1176, 2815) have well-constrained V_c (Figs A1 and A7), and therefore really are located closer to the spiral TFR.

5.1.2 *i-band TFR*

Fig. 7 presents the SDSS *i*-band TFR. The best fit to the Coma cluster spiral galaxy sample gives $M_i \propto (-7.04 \pm 0.45) \log V_c$, with a dispersion of 0.32 mag.

Our *i*-band TFR is similar to Pizagno et al. (2007), who calculate a gradient of -6.32 ± 0.22 and a dispersion of 0.42 mag, while Hall et al. (2012) report a steeper gradient (-8.71 ± 0.24). In addition, we compare to the recent I_C-band TFR relation presented by Tully & Courtois (2012), who use H I line widths of 267 galaxies in 13 clusters, including 23 spirals in the Coma cluster. For the Coma cluster, Tully & Courtois derive a TFR gradient of -6.96 ± 0.56, which is very similar to our value. For their full sample, they derive a gradient of -8.81 ± 0.16 (rms dispersion of 0.41 mag), which is more compatible with the Hall et al. TFR. Our shallower gradient in the *g* and *i* bands may result from a variation in the TFR between different clusters (as discussed by Bernstein et al. 1994). However, Tully & Courtois (2012) report that the Coma cluster sample can be drawn from the universal relation, and the variation may simply result from morphological selection bias in different environments.

We derive a mean *i*-band S0 TFR offset of 0.86 ± 0.19 mag, which is twice the rms dispersion of the spiral sample. This offset is smaller (by ~0.2 mag) than for the corresponding *g*-band TFR. The mean Coma S0 offsets from the Pizagno et al. (2007), Hall et al. (2012) and Tully & Courtois (2012) spiral TFRs are 0.83 ± 0.14, 1.23 ± 0.12 and 1.03 ± 0.14 mag, respectively (Table 7).

5.1.3 K_s*-band TFR*

The 2MASS K_s data are shallower than SDSS, restricting the S0 and spiral samples to 28 and 36 members, respectively (see Tables 6 and B2). The best fit to the Coma cluster spiral galaxies, shown in Fig. 8, reveals $M_{K_s} \propto (-7.31 \pm 0.49) \log V_c$, which is marginally steeper than in the *i* band. The rms dispersion of the spirals in M_{K_s} is 0.35 mag. The mean S0 offset in the K_s band is 0.83 ± 0.19 mag.

We compare our near-infrared TFR to the 2MASS Tully–Fisher Survey (Masters et al. 2008), which once again uses the SFI++ H I line widths (Springob et al 2007). For their full sample of 888 spiral galaxies, the authors use a bivariate best fit to derive a K_s-band gradient of -7.25 ± 0.11, with an rms dispersion of 0.40 mag. Attempting to correct for morphology (i.e. estimating the TFR of an Sc-only sample), they derive a much steeper gradient of -8.92 ± 0.10. Using the full Masters et al. spiral TFR as the reference for our Coma S0s, we calculate an offset of 0.80 ± 0.12 mag (Table 7).

Finally, we compare our K_s-band S0 TFR to Williams et al. (2010). Fig. 8 shows that their S0 TFR is very similar to the Coma cluster. However, these authors report a S0-to-spiral TFR offset of only 0.53 ± 0.15 mag. This smaller offset arises because their spiral

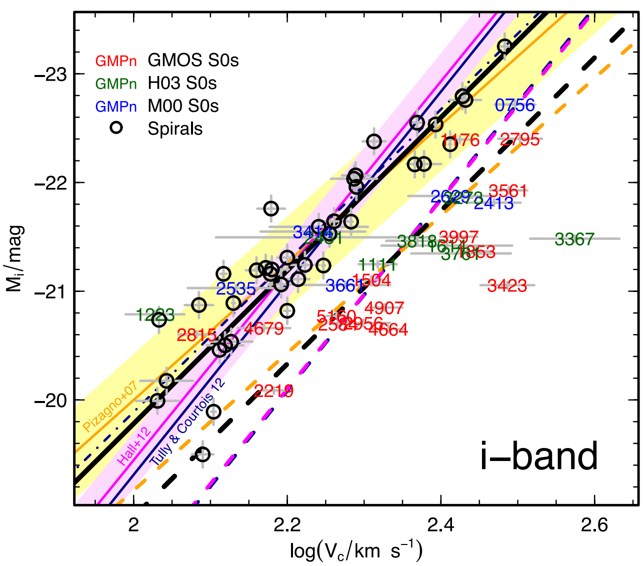

Figure 7. The *i*-band TFR for the Coma cluster. Layout identical to Fig. 6. The bivariate fit to the Coma spiral TFR has a gradient $= -7.04 \pm 0.45$, and the mean offset for the S0s is 0.86 ± 0.19 mag. The spiral TFRs from Pizagno et al. (2007, gradient $= -6.32 \pm 0.22$), Hall et al. (2012, gradient $= -8.71 \pm 0.24$) and Tully & Courtois (2012, gradient $= -8.81 \pm 0.16$) are shown by the orange, magenta and blue solid lines, respectively. The Coma-only sample from Tully & Courtois (2012, gradient $= -6.96 \pm 0.56$) is displayed as a blue dash–dotted line.

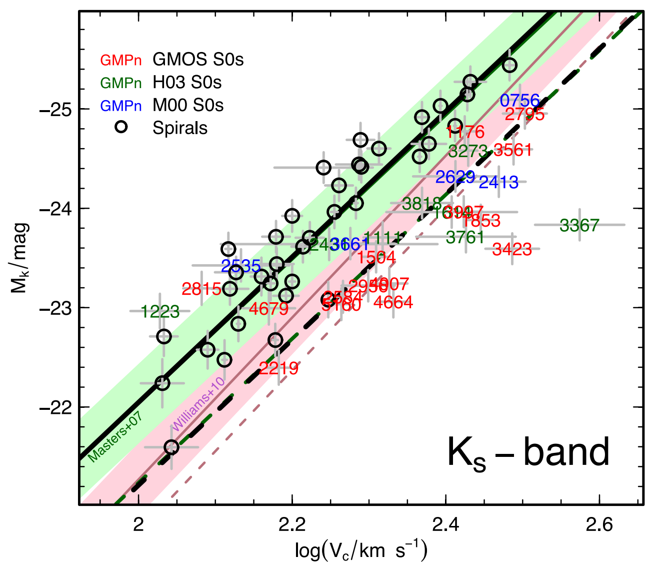

Figure 8. The K_s-band TFR for the Coma cluster. Layout as in Fig. 6. The fit to the Coma spiral TFR has a gradient $= -7.31 \pm 0.49$, and the mean offset for the S0 sample is 0.83 ± 0.19 mag. Spiral TFRs from Masters et al. (2007, gradient $= -7.25 \pm 0.11$) and Williams et al. (2010, gradient $= -8.15 \pm 0.76$) are shown by the green and mauve solid lines, respectively. While the green dashed line indicates the best fit to our Coma S0s using Masters et al. as the spiral reference, the mauve dashed line shows the S0 TFR directly from Williams et al. (2010).

TFR is significantly displaced from the spiral TFRs for either our Coma cluster sample or that of Masters et al. (∼0.6 mag; Table 6). The disagreement does not originate from luminosity, as each study uses 2MASS photometry with similar internal extinction corrections (≤0.1 mag). Nor is it due to different velocity systems: although the primary result from Williams et al. (plotted in Fig. 8) uses dynamic velocity derived from an NFW model of the dark matter mass distribution for each galaxy, their TFR is not significantly shifted if kinematic circular velocity is employed instead. The mean difference between these two velocities is 10 and 7 km s^{-1} for their spiral and S0 samples, respectively. Rather, the difference is due to the exclusive use of earlier types in the Williams et al. (2010) spiral sample (Sa–Sb only; and including several S0/a). In contrast, Sc–Sd spirals make up a third of our Coma cluster spiral sample. This clear offset of Sa/b spirals from much later types hints at a continuous trend in TFR offset, rather than discrete populations of spirals and S0s.

5.1.4 Simple model for the multiband TFR offsets

Generally, differences between spiral TFRs are due to sample selection (e.g. morphological bias) and population fitting procedures (as discussed in Hall et al. 2012). The typical S0 TFR offset in the Coma cluster is ∼0.8–1.2 mag, depending on the photometric band and selection criteria for the reference spiral TFR (Table 7). The i- and K_s-band fluxes are well correlated, with a colour dispersion of only 0.34 mag for spirals and 0.13 mag for S0s. In the g band, the S0 offset is ∼0.2 mag larger than for the redder bands.

Quantitatively, the size of the mean observed spiral-to-S0 offset, and its dependence on photometric band, is consistent with a simple model: S0s initially have similar star formation histories (SFHs) to the spirals, but are abruptly quenched at some intermediate redshift. As an example, we consider two variants of an exponentially decaying SFH, beginning 13 Gyr ago, and with an e-folding time (τ) of 14 Gyr. The first version is allowed to continue forming stars to the present day, while the second variant is cut off 5 Gyr before the present (i.e. $z \approx 0.5$). Convolving these SFHs with the Maraston (2005) single-burst models, we find that at $z = 0$ the quenched variant is 1.15 mag fainter in g than the unquenched version. The equivalent differences in i and K_s, which are less sensitive to the youngest stars, are 0.79 and 0.74 mag, respectively. These results are clearly consistent with the TFR offsets we observe, but they are not unique: other combinations of age, τ, and quenching time would also be compatible with the observations.

5.2 TFR offset correlations

In the previous section, we report that S0s are offset from the spiral TFR by an average of ∼0.8–1.2 mag, in the sense that S0s are fainter than spirals for a given rotational velocity. The existence and extent of the offset for any individual S0 in the Coma cluster are relatively independent of the choice of the reference spiral TFR or observed band. Simple models show that the TFR offset reflects a dimming of the stellar population, and can be interpreted as a probe of the time since the S0-to-spiral transformation began.

5.2.1 Correlation with colour

First, we explore the interplay between the TFR offset and the integrated optical colour of a galaxy. We begin by examining the SDSS $g-i$ colour–magnitude diagram for the full Coma cluster spectroscopic member sample (Fig. 9). The cluster members exhibit a strong red sequence (hereafter colour–magnitude relation, CMR) with an rms dispersion of 0.05 mag (e.g. Bower, Lucey & Ellis 1992; Smith et al. 2012a). By selection, the galaxies within our S0 sample are located in the vicinity of this CMR, and have only a marginally larger rms dispersion (0.07 mag). The spiral sample has bluer $g-i$ colours and a much larger rms dispersion (0.39 mag). While the two samples have similar luminosity distributions, the colour–magnitude diagram clearly displays the difference in colour. However, the populations do overlap in a ‘green valley’ region, which is often interpreted as the location for the evolutionary intermediate stage between star-forming late-type galaxies and quiescent early types (Faber et al. 2007). The offset from the CMR is an alternative tracer of the evolutionary progress of a galaxy.

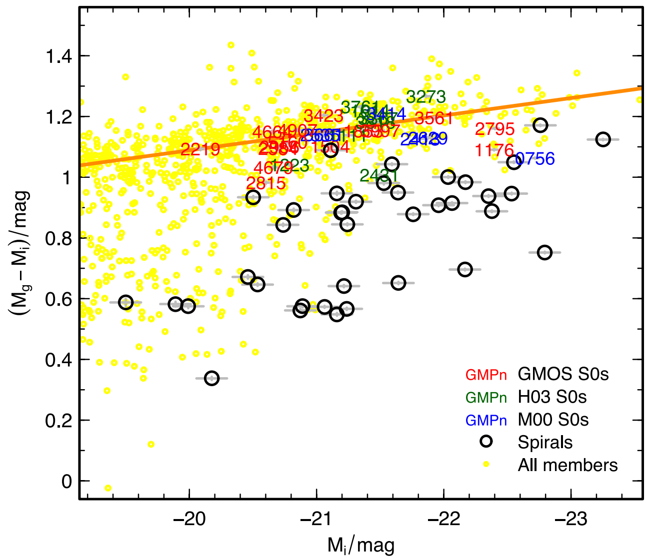

Figure 9. The $g-i$ colour–magnitude diagram for the full SDSS spectroscopic Coma cluster member sample (yellow circles) with the strong red sequence (colour–magnitude relation, CMR) highlighted via an orange line. By selection, our S0 galaxies are all located near to the CMR, while the spirals scatter to much bluer colours.

We compare the $g-i$ CMR offset to the i-band TFR offset in Fig. 10. The two parameters, almost by definition, have complementary interpretive power. The TFR offset is based on the tight spiral relation, offering little distinction within this population, while distributing the S0s over a 2 mag range. In contrast, the CMR offset is based on the tight red sequence for early types (including S0s), but shows a wide scatter in the spirals. Within the S0 population, there is a highly significant correlation between these offsets. S0s which are *fainter* than average for their rotational velocity are also *redder* than average for their luminosity. S0s with a colour most similar to ‘green valley’ spirals exhibit the smallest TFR offsets. The best bivariate fit to all S0s produces a gradient of 12.3 ± 1.9 (>6σ significance), with rms dispersions of 0.57 and 0.06 mag in the two axial directions. The three S0s falling significantly below the general trend (GMP1223, 2535, 3414) were previously identified as examples where the long-slit data may not measure the maximal V_c.

We now explore the interconnection of the TFR and CMR offsets by considering the likely SFHs of the S0 and spiral galaxies. Specifically, we investigate whether the same ‘parent’ population of spirals can give rise to both the (current) spirals and the (current) S0s in Coma, dependent only on whether or not they experienced

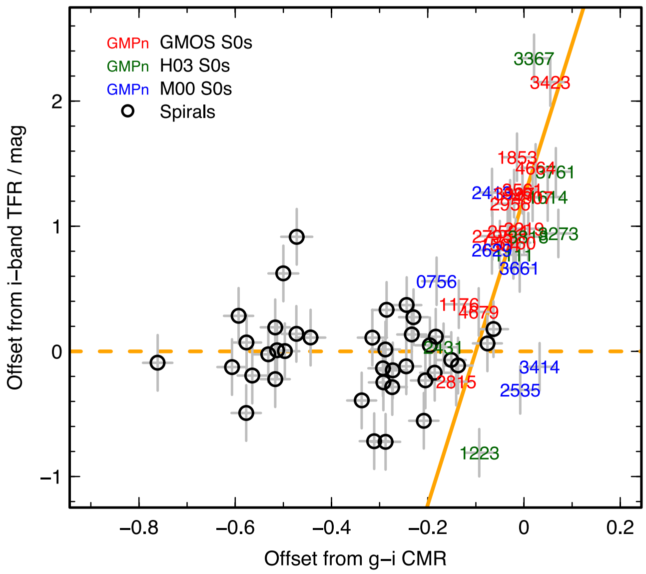

Figure 10. Relation between the offsets from the i-band TFR and the $g-i$ CMR. The solid orange line shows the best bivariate fit to all S0s (gradient =12.3 ± 1.9). S0s with larger TFR offsets show generally redder $g-i$ colours, while those closer to the spiral TFR also exhibit colours similar to the 'green valley' spirals.

instantaneous quenching at some intermediate epoch. We compare to predictions from both complex semi-analytic models and simple, quenched SFH models.

For the semi-analytic predictions, we use catalogues from the models of De Lucia & Blaizot (2007), which were based on merger trees from the Millennium Simulation (Springel et al. 2005). We use the virial velocity $V_{\rm vir}$ of the dark matter halo in place of $V_{\rm c}$, and applying a small offset of ∼0.25 mag to match the observed zero-point for the spiral TFR. [Note that models which attempt to compute $V_{\rm c}$ self-consistently fail to match the TFR zero-point, as discussed by Baugh (2006)]. Fig. 11 (left-hand panel) shows the model predictions for galaxies with bulge mass fractions less than 60 per cent, and with $V_{\rm vir} > 100\,{\rm km\,s^{-1}}$, and divided according to star formation rate (SFR). The general form of the distributions of star-forming and non-star-forming galaxies is well matched to the properties of the observed spirals and S0s, respectively. As in the observed sample, the region corresponding to small colour residuals and small TFR offsets is populated by a mixture of star-forming and non-star-forming galaxies. However, the colours of the simulated non-star-forming galaxies do not seem to be correlated with their TFR offsets, in contrast to the trend seen in the observed sample. This may be because the simple SFR cut cannot reproduce the morphological spiral/S0 distinction made in the observed samples, particularly for objects in transition between the classes.

The semi-analytic predictions include many physical processes, and perhaps obscure the effect of quenched SFHs on the residuals from both the CMR and TFR. To isolate this effect, we return to the simplified star formation model considered in Section 5.1.4. Here, the model library spans a range of formation times, (positive) exponential decline times, metallicities and quenching times in the past 5 Gyr. We generate predictions by convolving the library SFHs with the predictions for the single-burst models from Maraston (2005). For each galaxy in the Coma spiral sample, we find all *unquenched* models which at $z = 0$ match the observed $g-i$ colour. For each of these models, we extract predictions at $z = 0$ from the equivalent *quenched* models, for a range of quenching times. The loci displayed in Fig. 11 (right-hand panel) show the effect of instantaneous quenching at different epochs on a sample of hypothetical 'parent' spirals.

Fig. 11 (right-hand panel) demonstrates that this model can reproduce the location of most of the S0s by fading the predicted progenitors of the current spiral population: the observed spirals and S0s can all originate from the same 'parent' spiral population. However, we note that for the reddest S0s with large TFR offsets, the required quenching times are close to the epoch of 'formation'. The gradient of the upturn for these loci (as quenching time tends to formation time) may go some way to explain the observed S0 correlation between TFR and CMR offsets (Fig. 10). We emphasize that these calculations are very simplified (e.g. dust is neglected, we treat the whole galaxy with a single SFH ignoring any old 'bulge', no starbursts occur at quenching time, etc.), and more realistic models would likely have even more freedom to match the observed S0 properties.

5.2.2 *Evidence for environmental triggering*

The S0 TFR offset is consistent with abrupt quenching of a spiral population. We now explore the offset as a function of local environment. Galaxies at a larger projected distance from the cluster centre were accreted into the cluster (and its progenitors) at earlier times on average than galaxies projected near the cluster core (Gao et al. 2004; De Lucia et al. 2012; Smith et al. 2012a; Oman, Hudson & Behroozi 2013). Hence, cluster-centric radius can be employed as a proxy for infall time, albeit with substantial scatter.

The transformation of spirals into S0s could conceivably occur in small groups before infall into the cluster (pre-processing), where differential velocities are small and galaxy–galaxy interactions dominate the quenching process (e.g. Just et al. 2010). Alternatively, transformation could occur during infall into the cluster, where the cessation of star formation is triggered by the stripping of cold gas through interaction with the increasingly dense cluster medium (Gunn & Gott 1972; Abadi et al. 1999). Observational evidence of such stripping in the Coma cluster was reported by Smith et al. (2010). Naively, a correlation between local environment and time since quenching began may be expected only if the process occurred entirely within the cluster environment. However, recent evidence (Smith et al. 2012a) shows that galaxies at larger projected cluster-centric radii not only entered the cluster later on average than those near the centre, but also entered progenitor groups later as well. Therefore, even if quenching were triggered in smaller groups, radial trends would still be observed within the cluster.

We begin our discussion of the TFR offset with the i-band data, which has the higher photometric precision of SDSS and the smaller extinction-correction uncertainties. Fig. 12 presents the i-band TFR offset as a function of local environment, as traced by both the simple projected cluster-centric radius and the Σ density parameter. For the Coma cluster spiral sample, the mean offset is zero by definition, and the individual TFR offsets show no correlation with either density parameter. As emphasized previously, the spiral sample is located at much larger radii (lower densities) than the S0s.

By eye, the TFR offset for the S0 sample appears to have a strong trend with local environment, in the sense that most central S0s (located at highest density) exhibit the largest offset. However, statistically for the full S0 sample, this trend is not significant; the gradients are −0.34 ± 0.37 and 0.25 ± 0.25 versus log(radius) and log Σ, respectively. The four S0s with negative offsets, i.e. GMP1223, 2535, 2815, 3414, dilute the dominant trend that is

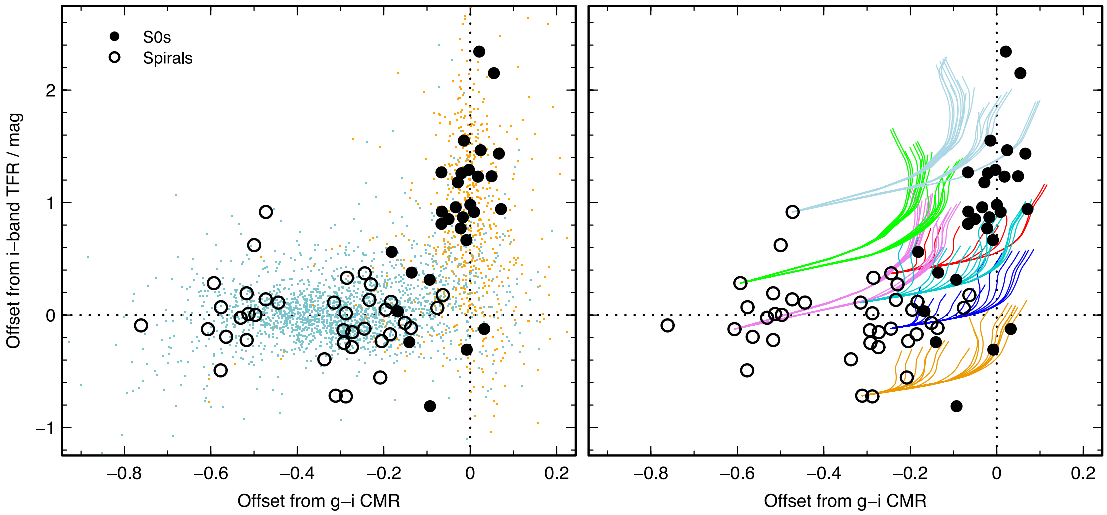

Figure 11. Relation between the offsets from the *i*-band TFR and the $g-i$ CMR, as in Fig. 10, with model predictions overplotted. Left: disc-dominated galaxies from semi-analytic models (De Lucia & Blaizot 2007), separated by SFR: non-star-forming galaxies (SFR $< 0.1\,\mathrm{M_{\odot}\,yr^{-1}}$) in orange and star-forming ones in blue. Right: single-burst star formation models from Maraston (2005). We select all unquenched model galaxies that match the observed optical colours of seven representative Coma spirals at $z = 0$. From the equivalent quenched models, we predict observables assuming a range of different quenching epochs. For example, the green lines show the possible $z = 0$ locations of model galaxies based on one example observed spiral, assuming a range of different SFHs, metallicities and quenching times. Hence, the lines are not evolutionary tracks, but the result of fading hypothetical 'parent' spirals via a range of models. These models can successfully reproduce the location of most observed Coma S0s.

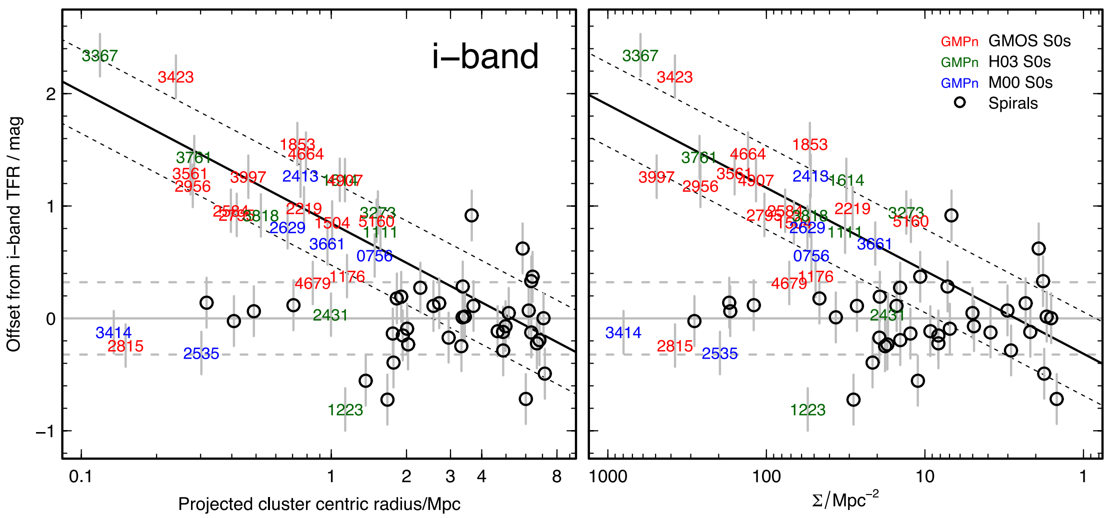

Figure 12. S0 offset from the *i*-band spiral TFR versus the projected cluster-centric radius (left) and the local density parameter Σ (right). The 1σ dispersion of the spiral galaxies (black circles; by definition, mean population offset = 0) is shown by the grey horizontal dashed lines. The S0s display a strong relationship between TFR offset and environment, with gradients of -1.17 ± 0.27 and 0.74 ± 0.17, respectively (solid black lines; 1σ dispersion = 0.37 mag, as black dotted lines), after removing four galaxies highlighted in previous sections (see the full explanation in Section 5.2).

apparent by eye. Three of these galaxies are the faintest S0s highlighted in Section 5.2.1, and may have underestimated V_c. The fourth (GMP2815) has an extremely low cz_{hel} ($4664\,\mathrm{km\,s^{-1}}$), indicating that the galaxy may be in the foreground: a projection-corrected radius parameter would place GMP2815 amongst the spiral population at a larger true cluster-centric radius. If we remove these four galaxies, the remaining 25 galaxies show a significant gradient ($>4\,\sigma$; solid black lines in Fig. 12) of -1.12 ± 0.26 and 0.70 ± 0.16 versus log(radius) and log Σ, respectively. The measured dispersion is 0.36 mag in both cases, with an intrinsic scatter of 0.32 mag. The majority of the spiral galaxies (∼60 per cent, not accounting for projection uncertainties) are also located within the 1σ limits of the S0 trend, indicating that there may indeed be a continuum of objects, or possibly an evolutionary track, linking the two populations.

In the g and K_s bands, we observe a similar trend in the S0s (not shown here for brevity). In the g band, the derived best-fitting gradients are -1.04 ± 0.27 and 0.64 ± 0.17 (versus projected radius and Σ, respectively), with 1σ dispersions of 0.37 and 0.38 mag (0.34 mag intrinsic scatter), after removing the same four outliers as identified above. In the near-infrared K_s band, the gradients are -1.12 ± 0.26 and 0.73 ± 0.16, with 1σ measured dispersion for either density parameter of 0.36 mag (0.27 mag intrinsic). In all three bands, there is a $>3\sigma$ correlation of the S0 TFR offset with the tracers of local density, consistent with each other within the uncertainties. This trend suggests a link between the onset of

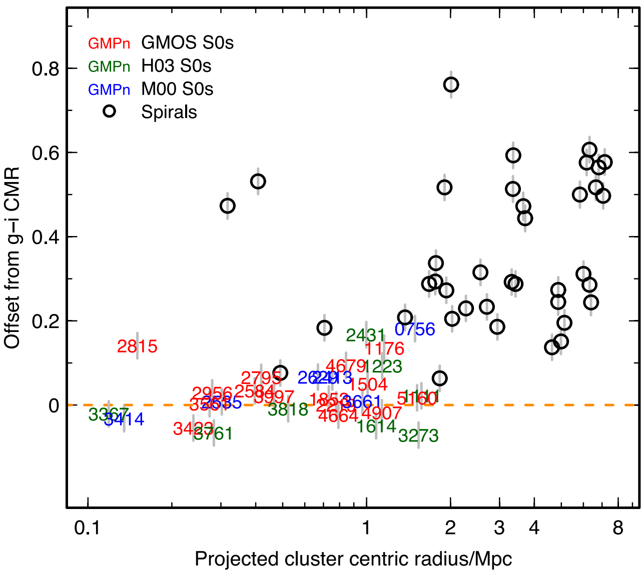

Figure 13. Offset from the $g-i$ CMR, as a function of projected cluster-centric radius. Generally, the mean CMR offset increases, with increasing scatter, as cluster radius decreases: for $\leq$0.5 Mpc ($\Sigma \geq 100\,\mathrm{Mpc}^{-2}$), the mean offset is 0.00 mag (0.05 mag rms scatter; including the obvious outlier GMP2815) and for >0.5 Mpc ($\Sigma < 100\,\mathrm{Mpc}^{-2}$), the mean offset is 0.05 mag (0.08 mag rms).

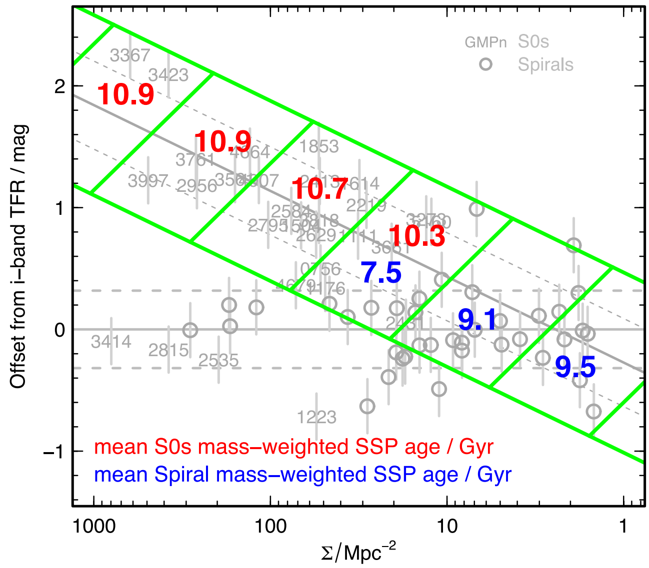

Figure 14. The mean mass-weighted simple stellar population (SSP) age (red/upper = S0s, blue/lower = spirals) binned along the correlation between projected local density Σ and offset from the i-band TFR (the best-fitting line shown in the right-hand panel of Fig. 12). The points representing S0 and spiral galaxies are displayed in grey to indicate the trend. The S0s show a marginal trend towards older ages with increasing Σ, while the spirals become younger, possibly indicating a central starburst.

interaction with the intracluster medium and the cessation of star formation.

For completeness, Fig. 13 presents the offset from the CMR as a function of local environment, as traced by the simple projected cluster-centric radius. The spiral population alone shows no trend with environment. Two blue spirals (GMP2559, GMP3896) appear to be near the cluster core (0.3–0.4 Mpc) but this is likely to be a projection effect. Within the S0 population there is a marginal trend, whereby the S0s at larger cluster radii exhibit an increased scatter (towards higher offsets; bluer colours) compared to S0s in the cluster core. S0s at $\leq$0.5 Mpc ($\Sigma \geq 100\,\mathrm{Mpc}^{-2}$) have a mean CMR offset of 0.00 mag and an rms scatter of 0.05 mag, whereas those at >0.5 Mpc ($\Sigma < 100\,\mathrm{Mpc}^{-2}$) exhibit a mean offset of 0.05 mag and a scatter of 0.08 mag. Generally, bluer S0s in the Coma cluster are more likely to be located at larger cluster-centric radii, much like the spiral sample itself, which is simply a confirmation of the morphology–density relation.

5.2.3 *Central age correlation*

A spiral infalling into a rich cluster will encounter the increasing density of the intracluster medium and this may trigger quenching. A pure fading model of S0 transformation would necessarily increase the average stellar population age. If quenching is accompanied by a nuclear starburst, the central age of more recently quenched galaxies would be even younger, strengthening any age–TFR offset correlation for bulge-dominated ages. For a small sample of Fornax cluster galaxies, Bedregal et al. (2006b) report that central ages are more strongly correlated with the TFR offset than the 'global' ages. In this final section, we briefly attempt to constrain the transformation mechanism in Coma via single stellar population ages derived from the VErsatile SPectral Analysis (VESPA) catalogue[5] based on SDSS DR7 spectra (Tojeiro et al. 2009). The catalogue includes all of the Coma cluster members in our S0 and spiral samples, and describes SFH via discrete stellar mass estimates in several stellar age bins. From this information, we calculate the mass-weighted stellar population age

$$\langle \mathrm{Age} \rangle_{\mathcal{M}} = \sum_i \left(\mathrm{Age}_i \mathcal{M}_i\right) / \sum_i \mathcal{M}_i, \qquad (9)$$

where Age_i and $\mathcal{M}_i$ are the age and estimated stellar mass in the ith bin. The 3 arcsec SDSS fibres ensure that for Coma, the mass-weighted stellar population age simply reflects the typical SFH of the central ~1.4 kpc of the bulge.

In Fig. 12, we reported the trend between TFR offset and local projected density for S0s. In bins along this correlation, we now determine the mean ages of the spiral and S0 populations (Fig. 14). The S0 population shows a very marginal trend of increasing age (10.3 to 10.9 Gyr) with increasing local density, in agreement with Smith et al. (2012a), although the age uncertainty in each bin is ~1 Gyr. Interestingly, the spiral sample exhibits the opposite trend: decreasing age (9.5 to 7.5 Gyr) with increasing local density. This may be indicative of a central starburst in the early stages of the transformation, before quenching in the disc transforms the observed morphology from spiral to S0.

6 CONCLUSIONS

In order to characterize early-type disc galaxies in the rich cluster environment, we have undertaken deep, long-slit spectroscopy with GMOS of 15 Coma cluster S0s. From absorption line measurements, we have determined kinematic properties along the major axis to several times the disc scalelength, and hence derived rotation curves. We have supplemented our kinematic measurements with literature data from M00 and H03, yielding a combined sample of

[5] http://www-wfau.roe.ac.uk/vespa/

29 Coma cluster S0s. Using SDSS and 2MASS photometry, we have investigated the TFR for cluster S0s.

We confirm the existence of a TF offset for S0 galaxies, calculating that, at fixed rotational velocity, S0s are fainter than spirals by an average 1.06 ± 0.18, 0.85 ± 0.19 and 0.86 ± 0.18 mag in the g, i and K_s bands, respectively. The TFR offsets are consistent with a simple star formation model in which S0s initially have similar SFHs to the spirals, but are abruptly quenched at some intermediate redshift. The TFR offset can be interpreted as a tracer of the time since the cessation of star formation, and exhibits a strong correlation ($>6\sigma$) with the residual from the optical CMR. Typically, S0s which are fainter than average for their rotational velocity are also redder than average for their luminosity.

The S0s in our study span a wide range of local densities within the Coma cluster, which has allowed environmental trends to be investigated. We find a correlation between the TFR offset and environment, in the sense that S0s located in regions of lower local density are closer to the spiral TFR. Since current cluster-centric radius is related to time since accretion into the cluster (or its progenitors), the correlation of TFR offset with the radius suggests that the transformation of spirals into S0s is associated with cluster infall. We also observe a decrease in the mean stellar population age of spirals with increasing local density, which may indicate that immediately prior to quenching in the disc, the transformative process includes a burst of star formation in the bulge.

In future papers, we will present absorption line index profiles for the 15 GMOS S0s. The long-slit observations were specifically designed to enable stellar population analysis at radii beyond several disc scalelengths. Examination of such gradients (e.g. Rawle, Smith & Lucey 2010) from both bulge and disc components, in conjunction with *GALEX* ultraviolet colours tracing recent star formation (Rawle et al. 2008; Smith, Lucey & Carter 2012b), will allow further constraints to be put on the S0 transformation process.

ACKNOWLEDGEMENTS

The authors are grateful to Richard Bower for useful discussion while preparing this manuscript.

TDR is supported by a Research Fellowship at the European Space Agency (ESA). JRL and RJS are supported by STFC Rolling Grant PP/C501568/1 ‘Extragalactic Astronomy and Cosmology at Durham 2008–2013’. JTCGH is supported by an STFC studentship.

This work is based on observations obtained at the Gemini Observatory, which is operated by the Association of Universities for Research in Astronomy, Inc., under a cooperative agreement with the NSF on behalf of the Gemini partnership: the National Science Foundation (US), the National Research Council (Canada), CONICYT (Chile), the Australian Research Council (Australia), Ministrio da Cincia, Tecnologia e Inovao (Brazil) and Ministerio de Ciencia, Tecnolog'a e Innovacin Productiva (Argentina). At the time of observation, the Gemini partnership also included the Science and Technology Facilities Council (UK), who supported TDR as a visiting astronomer at Gemini North in 2009 March.

This publication also makes use of data products from the Two Micron All Sky Survey, which is a joint project of the University of Massachusetts and the Infrared Processing and Analysis Center/California Institute of Technology, funded by NASA and the National Science Foundation. Funding for SDSS-III has been provided by the Alfred P. Sloan Foundation, the Participating Institutions, the National Science Foundation and the US Department of Energy Office of Science. The SDSS-III website is http://www.sdss3.org/. The Millennium Simulation data bases used in this paper and the web application providing online access to them were constructed as part of the activities of the German Astrophysical Virtual Observatory. This research has made use of the NASA/IPAC Extragalactic Database (NED) which is operated by the Jet Propulsion Laboratory, California Institute of Technology, under contract with the National Aeronautics and Space Administration.

REFERENCES

Abadi M. G., Moore B., Bower R. G., 1999, MNRAS, 308, 947
Ahn C. P. et al., 2012, ApJS, 203, 21
Baldry I. K., Balogh M. L., Bower R. G., Glazebrook K., Nichol R. C., Bamford S. P., Budavari T., 2006, MNRAS, 373, 469
Baugh C. M., 2006, Rep. Prog. Phys., 69, 3101
Bedregal A. G., Aragón-Salamanca A., Merrifield M. R., Milvang-Jensen B., 2006a, MNRAS, 371, 1912
Bedregal A. G., Aragón-Salamanca A., Merrifield M. R., 2006b, MNRAS, 373, 1125
Bekki K., 1999, ApJ, 510, 15
Bernstein G. M., Guhathakurta P., Raychaudhury S., Giovanelli R., Haynes M. P., Herter T., Vogt N. P., 1994, AJ, 107, 1962
Blanton M. R., Roweis S., 2007, AJ, 133, 743
Boselli A., Gavazzi G., 2006, PASP, 118, 517
Bower R. G., Lucey J. R., Ellis R. S., 1992, MNRAS, 254, 601
Bundy K. et al., 2010, ApJ, 719, 1969
Burstein D., Ho L. C., Huchra J. P., Macri L. M., 2005, ApJ, 621, 246
Capellari M., Emsellem E., 2004, PASP, 116, 138
Catinella B., Haynes M. P., Giovanelli R., 2007, AJ, 134, 334
Christlein D., Zabludoff A. I., 2004, ApJ, 616, 192
Cortesi A. et al., 2013, MNRAS, 432, 1010
Courteau S., 1997, AJ, 114, 2402
Courteau S., Dutton A. A., van den Bosch F. C., MacArthur L. A., Dekel A., McIntosh D. H., Dale D. A., 2007, ApJ, 671, 203
Davis T. A. et al., 2011, MNRAS, 414, 968
De Lucia G., Blaizot J., 2007, MNRAS, 375, 2
De Lucia G., Weinmann S., Poggianti B. M., Aragon-Salamanca A., Zaritsky D., 2012, MNRAS, 423, 1277
De Vaucouleurs G., De Vaucouleurs A., Corwin H. G., Jr, Buta R. J., Paturel G., Fouque P., 1991, Third Reference Catalogue of Bright Galaxies. Springer, New York
Dressler A., 1980a, ApJS, 42, 565 (D80)
Dressler A., 1980b, ApJ, 236, 351
Dressler A., Sandage A., 1983, ApJ, 265, 664
Dressler A., Lynden-Bell D., Burstein D., Davies R. L., Faber S. M., Terlevich R., Wegner G., 1987, ApJ, 313, 42
Dressler A. et al., 1997, ApJ, 490, 577
Faber S. M. et al., 2007, ApJ, 665, 265
Gao L., De Lucia G., White S. D. M., Jenkins A., 2004, MNRAS, 352, 1
Geach J. E., Smail I., Moran S. M., Treu T., Ellis R. S., 2009, ApJ, 691, 783
Godwin J. G., Metcalfe N., Peach J. V., 1983, MNRAS, 202, 113
Gunn J. E., Gott J. R., 1972, ApJ, 176, 1
Hall M., Courteau S., Dutton A. A., McDonald M., Zhu Y., 2012, MNRAS, 425, 2741
Hinz J. L., Rieke G. H., Caldwell N., 2003, AJ, 126, 2622 (H03)
Hook I. M., Jørgensen I., Allington-Smith J. R., Davies R. L., Metcalfe N., Murowinski R. G., Crampton D., 2004, PASP, 116, 425
Jarrett T. H., Chester T., Cutri R., Schneider S., Skrutskie M., Huchra J. P., 2000, AJ, 119, 2498
Jarrett T. H. et al., 2013, AJ, 145, 6
Just D. W., Zaritsky D., Sand D. J., Desai V., Rudnick G., 2010, ApJ, 711, 192
Kaviraj S. et al., 2012, MNRAS, 423, 49
Larson R. B., Tinsley B. M., Caldwell C. N., 1980, ApJ, 237, 692
Maraston C., 2005, MNRAS, 362, 799
Masters K. L., Giovanelli R., Haynes M. P., 2003, AJ, 126, 158

Masters K. L., Springob C. M., Haynes M. P., Giovanelli R., 2006, ApJ, 653, 861
Masters K. L., Springob C. M., Huchra J. P., 2008, AJ, 135, 1738
McCarthy I. G., Frenk C. S., Font A. S., Lacey C. G., Bower R. G., Mitchell N. L., Balogh M. L., Theuns T., 2008, MNRAS, 383, 593
Mehlert D., Saglia R. P., Bender R., Wegner G., 2000, A&A, 141, 449 (M00)
Mocz P., Green A., Malacari M., Glazebrook K., 2012, MNRAS, 425, 296
Moorthy B. K., Holtzman J. A., 2006, MNRAS, 371, 583
Moran S. M., Ellis R. S., Treu T., Smith G. P., Rich R. M., Smail I., 2007, ApJ, 671, 1503
Morelli L. et al., 2008, MNRAS, 389, 341
Neistein E., Maoz D., Rix H.-W., Tonry J. L., 1999, AJ, 117, 2666
Norris M. A., Sharples R. M., Kuntschner H., 2006, MNRAS, 367, 815
Oman K. A., Hudson M. J., Behroozi P. S., 2013, MNRAS, 431, 2307
Peng C. Y., Ho L. C., Impey C. D., Rix H.-W., 2010, AJ, 139, 2097
Pizagno J. et al., 2007, AJ, 134, 945
Poggianti B. M. et al., 2001, ApJ, 563, 118
Rawle T. D., Smith R. J., Lucey J. R., Hudson M. J., Wegner G. A., 2008, MNRAS, 385, 2097
Rawle T. D., Smith R. J., Lucey J. R., 2010, MNRAS, 401, 852
Rawle T. D. et al., 2012, ApJ, 756, 106
Raychaudhury S., von Braun K., Bernstein G. M., Guhathakurta P., 1997, AJ, 113, 2046
Sandage A., 2005, ARA&A, 43, 581
Schlegel D. J., Finkbeiner D. P., Davis M., 1998, ApJ, 500, 525
Smith R. J., Lucey J. R., Hudson M. J., 2009, MNRAS, 400, 1690
Smith R. J. et al., 2010, MNRAS, 408, 1417
Smith R. J., Lucey J. R., Price J., Hudson M. J., Phillipps S., 2012a, MNRAS, 419, 3167
Smith R. J., Lucey J. R., Carter D., 2012b, MNRAS, 421, 2982
Smith M. W. L. et al., 2012c, ApJ, 748, 123
Springel V. et al., 2005, Nat, 435, 629
Springob C. M., Masters K. L., Haynes M. P., Giovanelli R., Marinoni C., 2007, ApJS, 172, 599
Thomas D., Davies R. L., 2006, MNRAS, 366, 510
Tojeiro R., Wilkins S., Heavens A. F., Panter B., Jimenez R., 2009, ApJS, 185, 1
Tully R. B., Courtois H. M., 2012, ApJ, 749, 78
Tully R. B., Fisher J. R., 1977, A&A, 54, 661
Tully R. B., Pierce M. J., 2000, ApJ, 533, 744
Tully R. B., Pierce M. J., Huang J.-S., Saunders W., Verheijen M. A. W., Witchalls P. L., 1998, AJ, 115, 2264
Williams M. J., Bureau M., Cappellari M., 2009, MNRAS, 400, 1665
Williams M. J., Bureau M., Cappellari M., 2010, MNRAS, 409, 1330
Wilman D. J., Oemler A., Mulchaey J. S., McGee S. L., Balogh M. L., Bower R. G., 2009, ApJ, 692, 298

APPENDIX A: PHOTOMETRIC AND KINEMATIC PROFILES FOR THE GMOS S0 GALAXIES

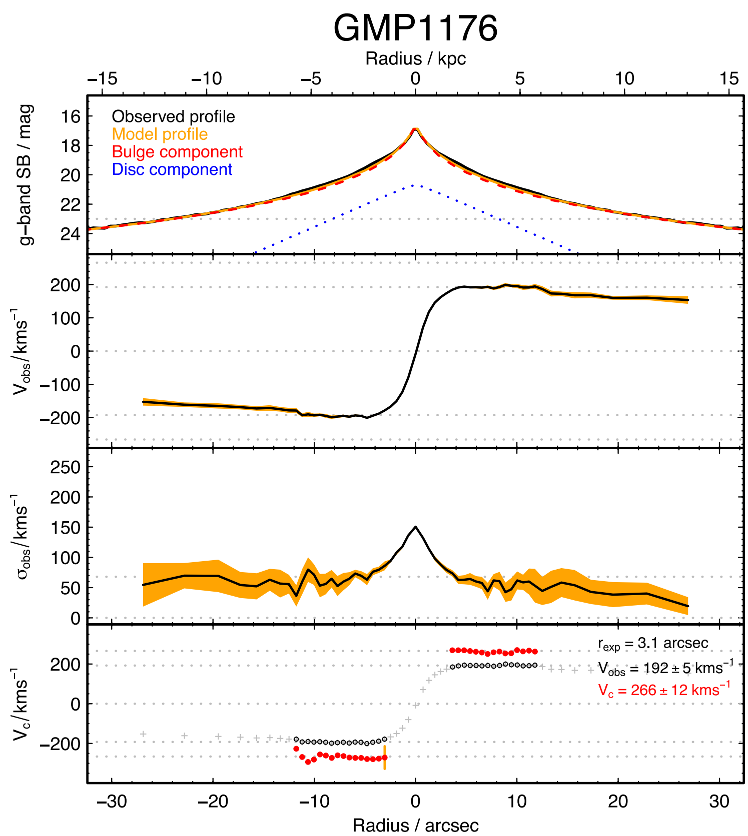

Figure A1. Photometric and kinematic profiles for GMP1176. All *x*-axes are delineated in arcsec, apart from the very top axis which indicates the corresponding physical scale in kpc (1 arcsec = 0.48 kpc at the distance of Coma). Uppermost panel: observed *g*-band surface brightness profile (black solid line). GALFIT two-component decomposition model surface brightness is also shown for the Sérsic bulge (red dashes), exponential disc (blue dots) and total profile (orange solid). Central panels: observed rotational velocity (V_{obs}) and velocity dispersion (σ_{obs}). 1σ errors are indicated by orange shading. Lowermost panel: the open black circles show observed velocities, and the filled red circles show the circular rotation velocity in the flat turnover region of the radial profile (V_c, see the text for details). The maximum values of V_{obs} and V_c are given in the top right of the panel, along with the exponential disc scalelength.

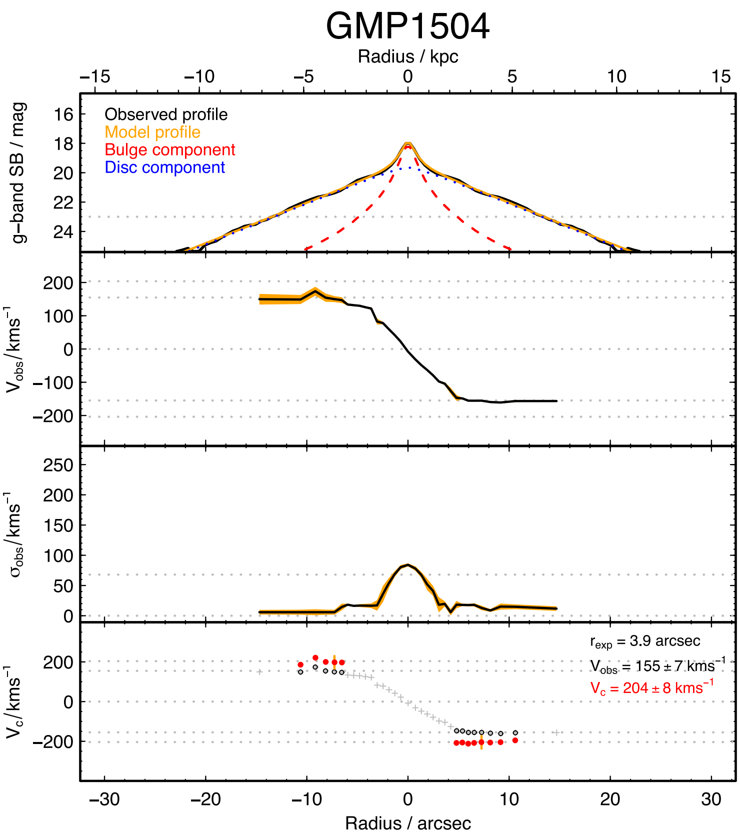

Figure A2. Photometric and kinematic profiles for GMP1504. Layout as in Fig. A1.

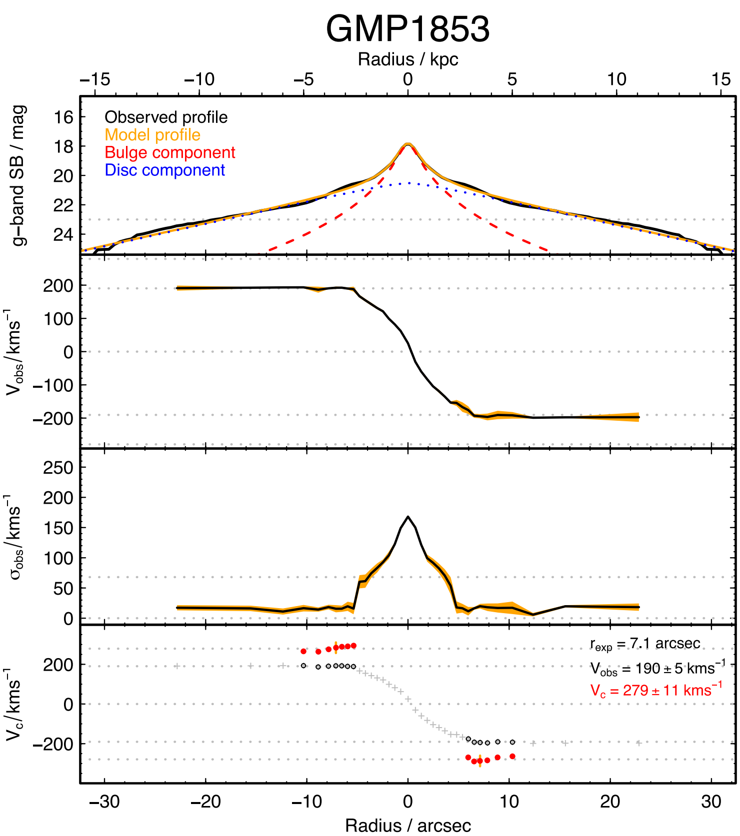

Figure A3. Photometric and kinematic profiles for GMP1853. Layout as in Fig. A1.

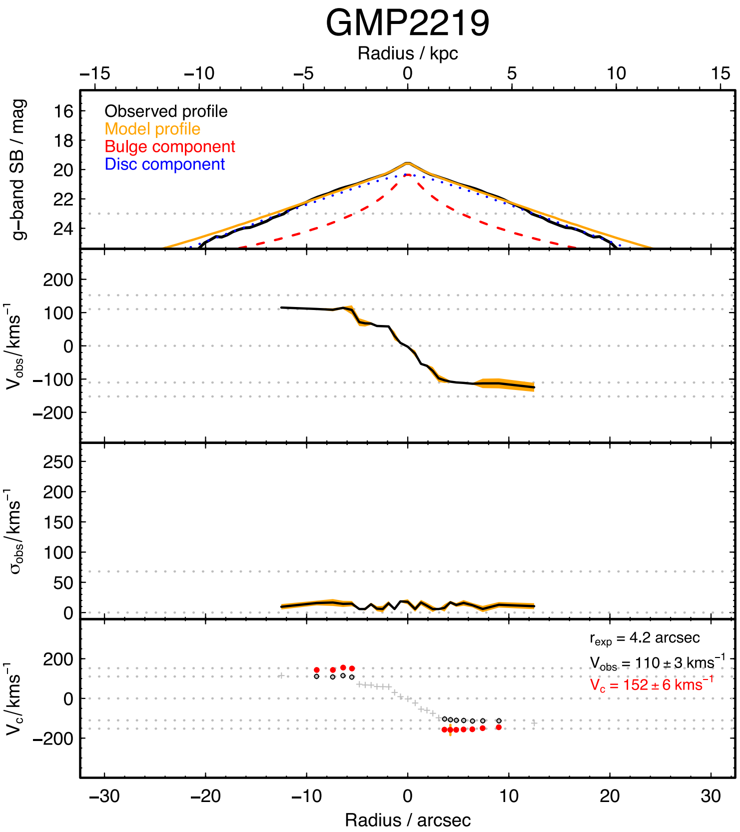

Figure A4. Photometric and kinematic profiles for GMP2219. Layout as in Fig. A1.

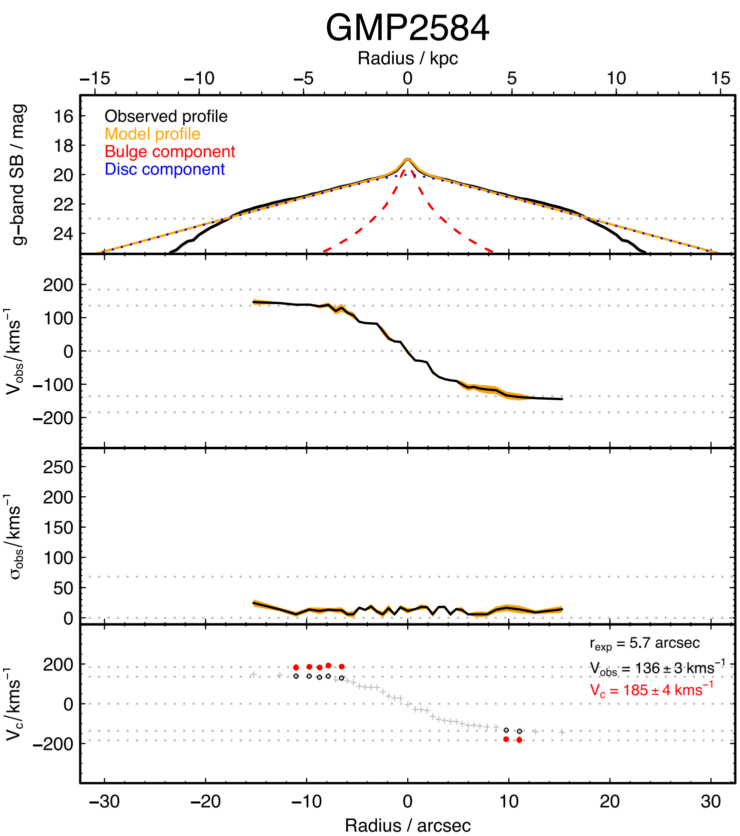

Figure A5. Photometric and kinematic profiles for GMP2584. Layout as in Fig. A1.

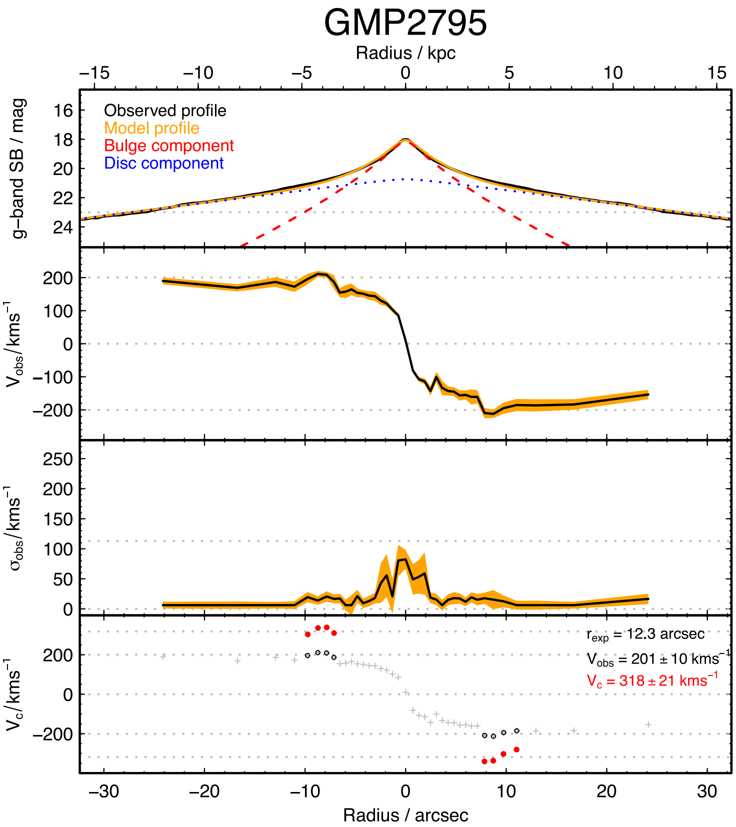

Figure A6. Photometric and kinematic profiles for GMP2795. Layout as in Fig. A1.

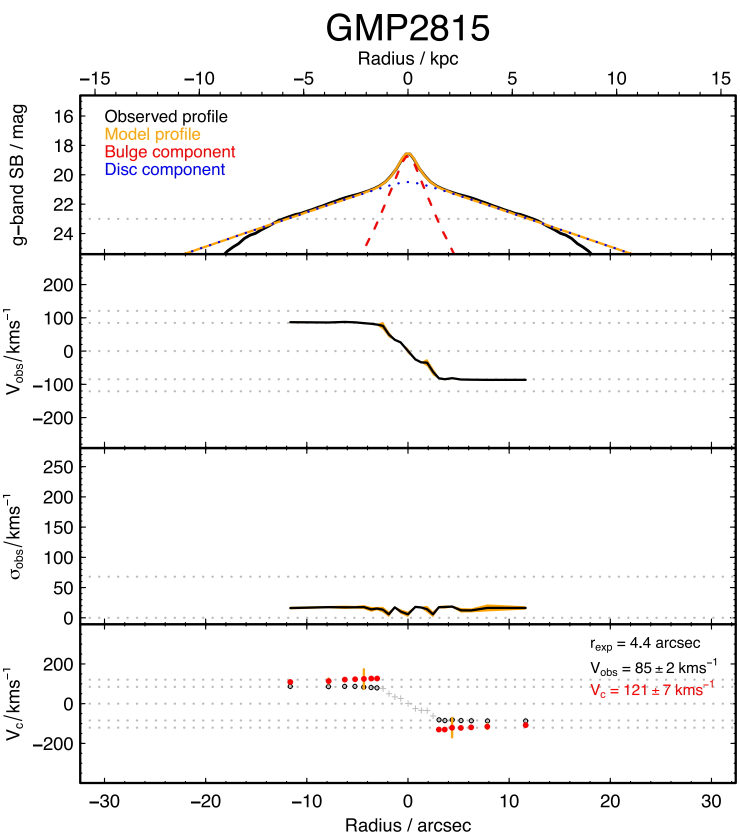

Figure A7. Photometric and kinematic profiles for GMP2815. Layout as in Fig. A1.

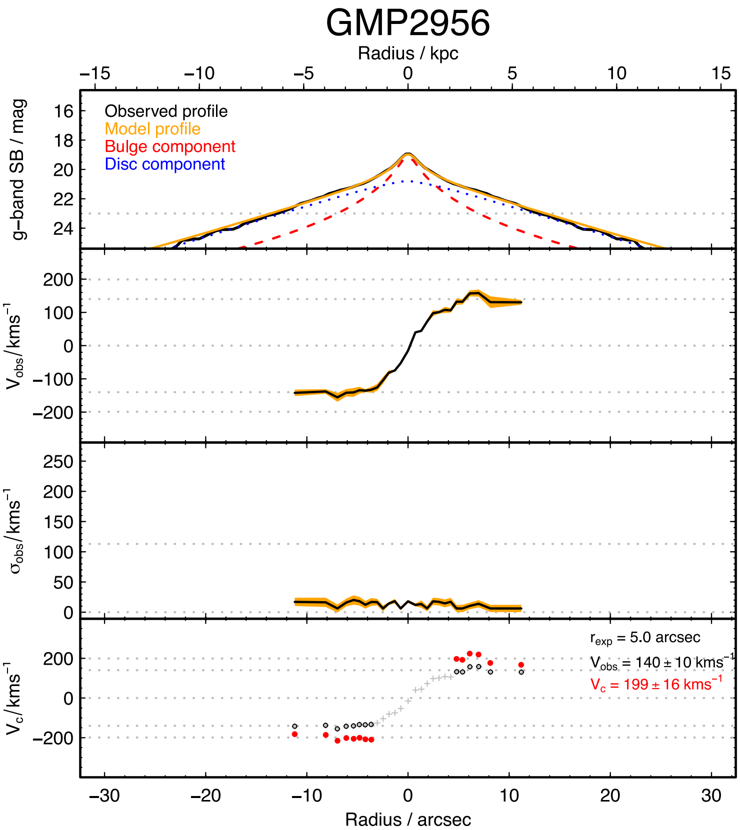

Figure A8. Photometric and kinematic profiles for GMP2956. Layout as in Fig. A1.

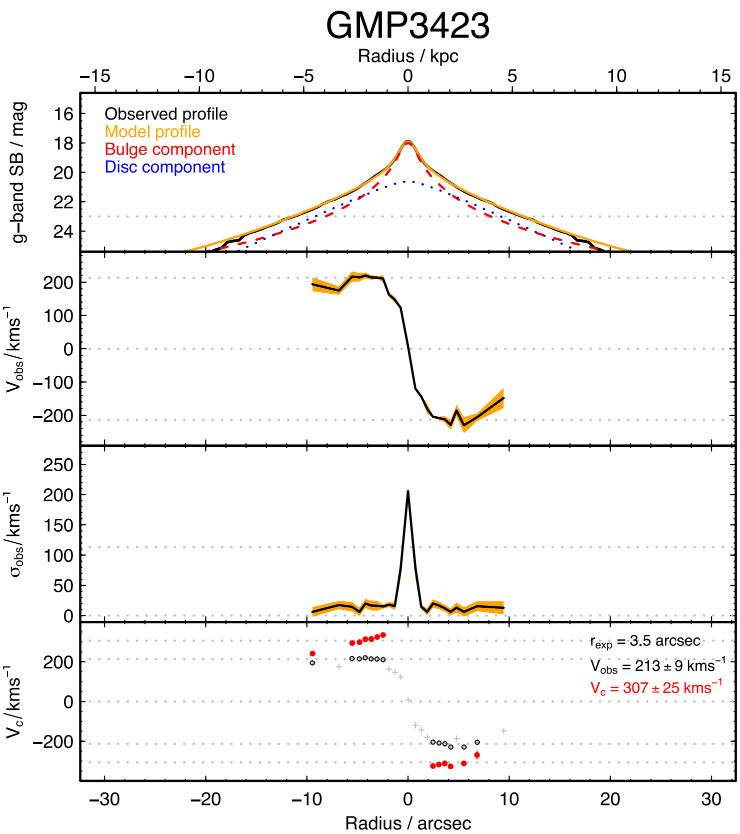

Figure A9. Photometric and kinematic profiles for GMP3423. Layout as in Fig. A1.

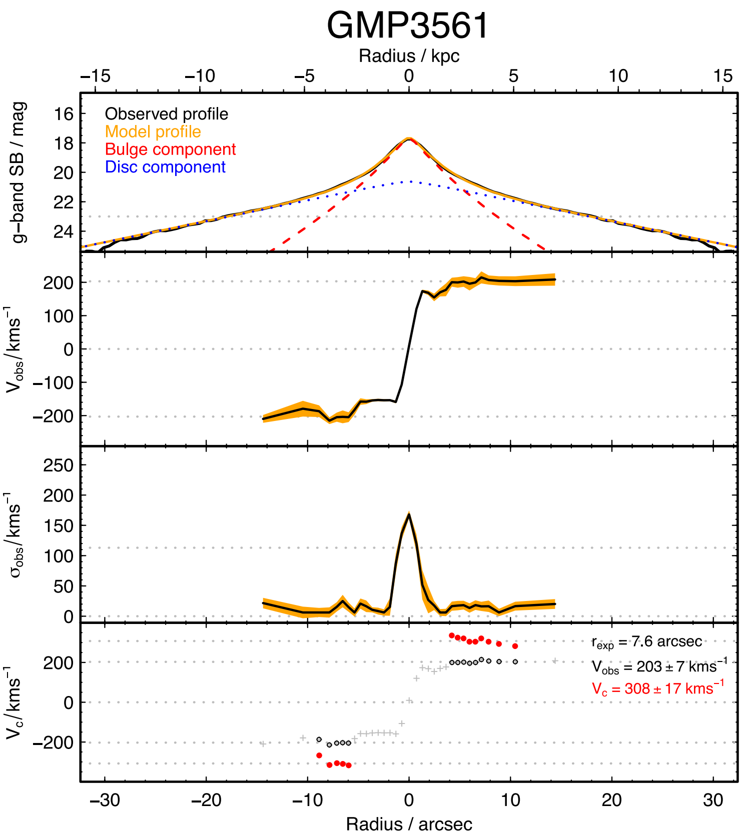

Figure A10. Photometric and kinematic profiles for GMP3561. Layout as in Fig. A1.

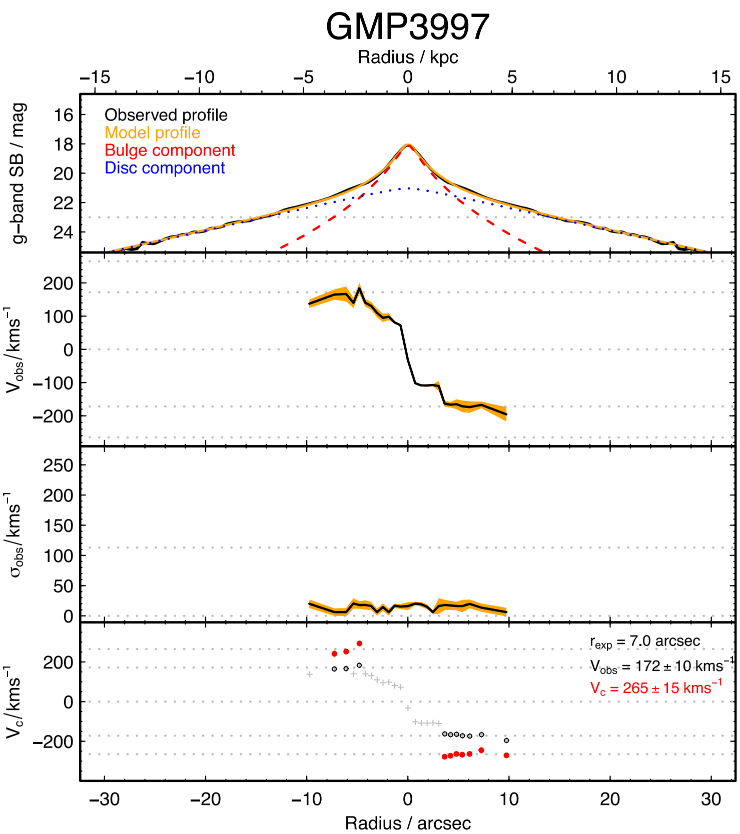

Figure A11. Photometric and kinematic profiles for GMP3997. Layout as in Fig. A1.

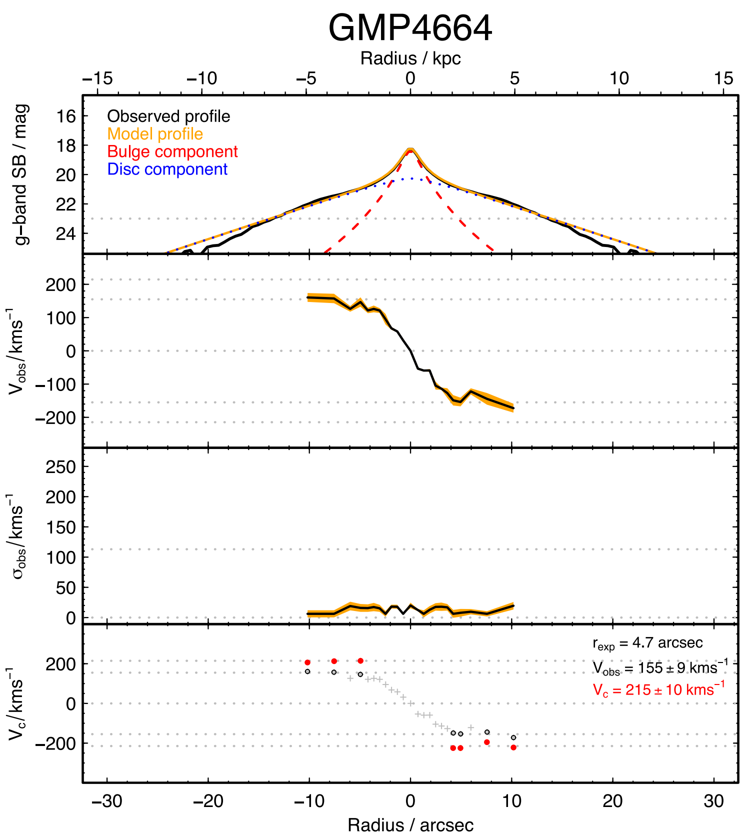

Figure A12. Photometric and kinematic profiles for GMP4664. Layout as in Fig. A1.

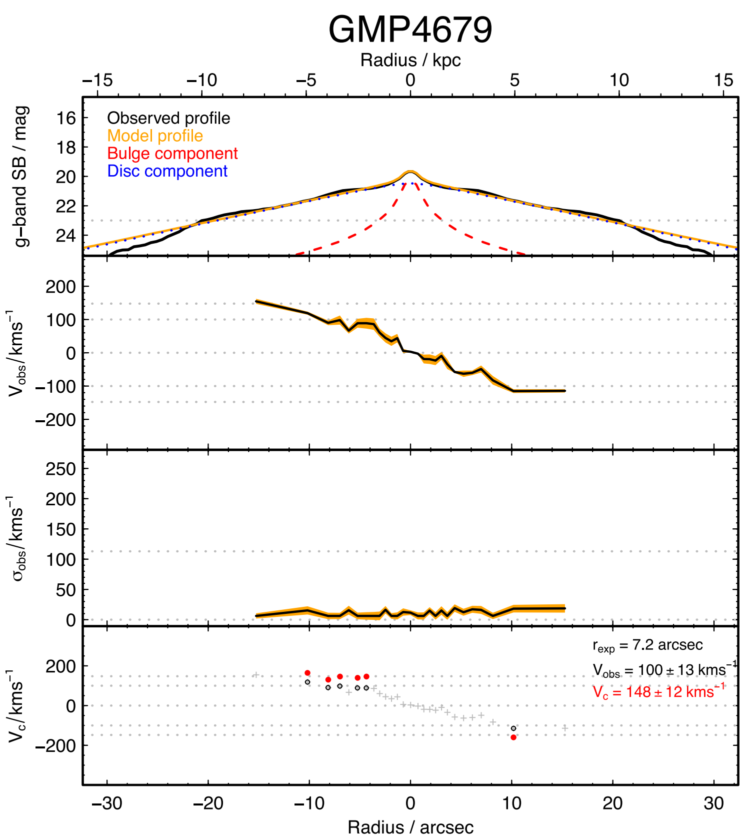

Figure A13. Photometric and kinematic profiles for GMP4679. Layout as in Fig. A1.

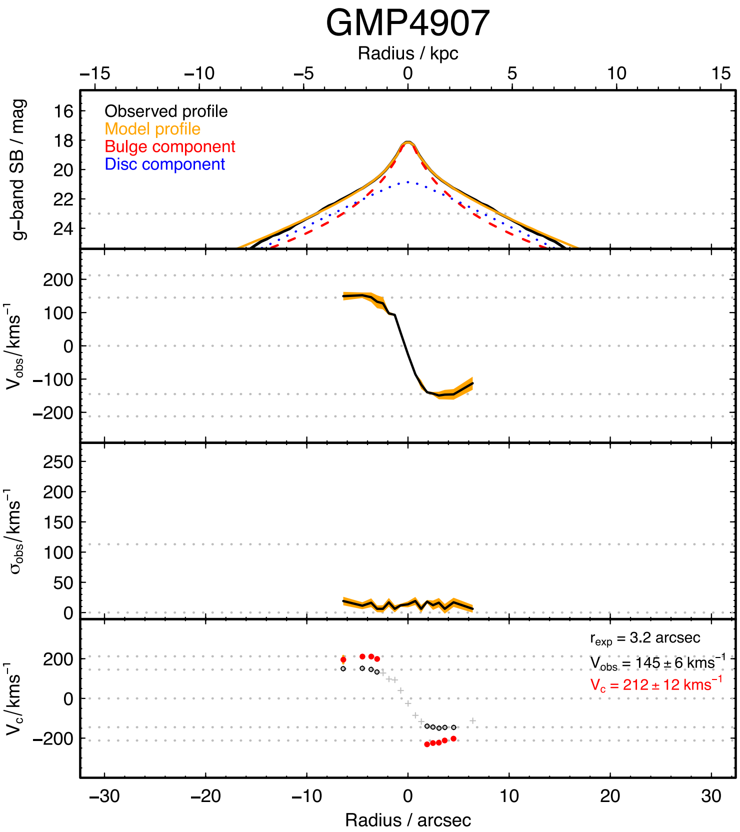

Figure A14. Photometric and kinematic profiles for GMP4907. Layout as in Fig. A1.

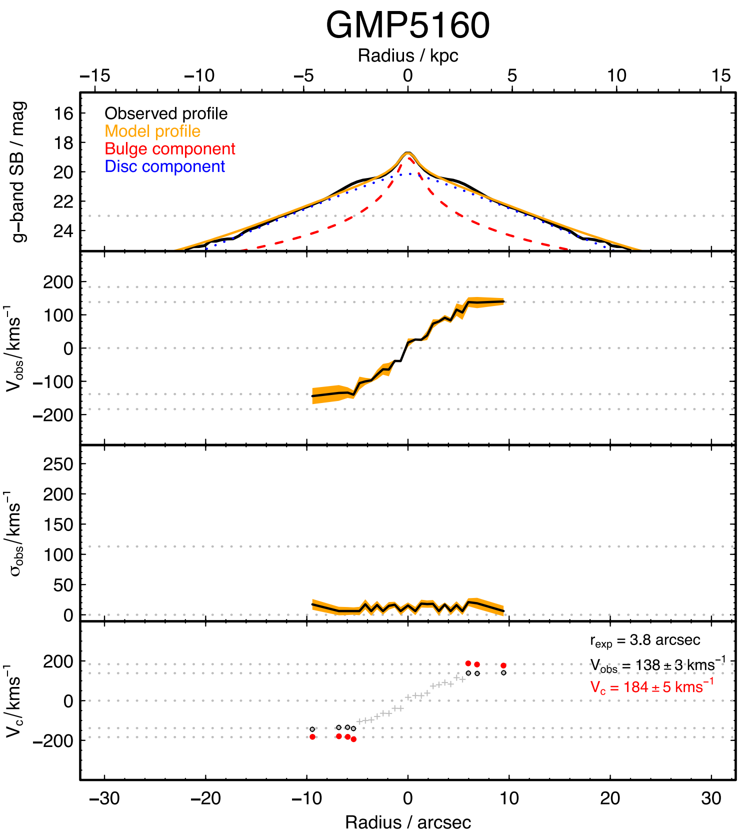

Figure A15. Photometric and kinematic profiles for GMP5160. Layout as in Fig. A1.

APPENDIX B: COMA CLUSTER SPIRAL GALAXY SAMPLE

Table B1. Observed quantities for the 38[a] Coma spiral galaxy sample introduced in Section 4.2. Position and optical photometric from SDSS (AB mags). K_s band from 2MASS (Vega mags). CMB frame velocity (cz_{CMB} km s^{-1}), line width and inclination from Springob et al (2007).

GMP ID	U/AGC #	RA (J2000)	Dec. (J2000)	m_g (mag)	m_i (mag)	m_{K_s} (mag)	cz_{CMB} (km s^{-1})	log$W$	i (deg)
–	7845	190.318 16	27.853 15	15.128 ± 0.003	14.391 ± 0.003	12.40 ± 0.09	8014	2.431	78.0
–	7877	190.696 66	27.271 93	15.689 ± 0.004	14.577 ± 0.003	11.97 ± 0.07	6186	2.501	84.0
–	7890	190.772 31	27.714 06	14.750 ± 0.002	14.095 ± 0.003	12.02 ± 0.08	7802	2.493	46.8
–	7955	191.796 75	26.710 83	15.113 ± 0.003	13.901 ± 0.003	11.27 ± 0.07	7034	2.556	81.0
–	221022	191.868 21	27.457 78	14.772 ± 0.002	13.620 ± 0.002	10.74 ± 0.04	6885	2.542	56.7
–	221033	192.175 30	26.417 30	15.108 ± 0.003	14.013 ± 0.003	11.31 ± 0.05	7137	2.501	76.2
–	8004	192.908 20	31.352 76	14.773 ± 0.004	14.089 ± 0.003	12.51 ± 0.06	6445	2.479	68.1
–	8013	193.151 21	26.749 88	14.918 ± 0.003	14.147 ± 0.003	12.16 ± 0.10	8157	2.548	78.0
–	8025	193.510 33	29.603 61	14.391 ± 0.002	13.111 ± 0.002	10.20 ± 0.03	6583	2.694	86.3
GMP5422	221130	194.119 07	27.291 27	15.261 ± 0.003	14.366 ± 0.003	12.42 ± 0.13	7796	2.334	46.9
GMP5234	221147	194.206 89	27.093 91	15.400 ± 0.003	14.165 ± 0.002	11.58 ± 0.05	7117	2.515	69.7
GMP5197	221149	194.210 89	28.929 83	15.082 ± 0.003	14.058 ± 0.002	11.76 ± 0.05	8297	2.481	70.3
GMP5006	8069	194.297 49	29.045 08	14.432 ± 0.002	13.273 ± 0.002	10.75 ± 0.03	7927	2.588	67.1
–	221174	194.380 02	26.512 15	15.096 ± 0.003	14.078 ± 0.002	11.51 ± 0.05	7533	2.524	72.7
GMP4437	221206	194.538 44	28.708 56	15.159 ± 0.004	14.077 ± 0.004	11.62 ± 0.06	7881	2.418	73.3
GMP3896	8096	194.733 08	27.833 37	14.755 ± 0.003	13.842 ± 0.003	11.01 ± 0.04	7803	2.562	87.1
GMP2987	8108	195.014 70	26.898 11	14.219 ± 0.002	13.089 ± 0.002	10.63 ± 0.03	6173	2.614	80.1
GMP2582	221402	195.148 65	27.574 22	15.801 ± 0.003	14.734 ± 0.003	12.02 ± 0.06	5389	2.420	74.0
GMP2559	221406	195.157 75	28.057 97	15.437 ± 0.003	14.674 ± 0.003	11.84 ± 0.05	7896	2.428	68.1
GMP2544	8118	195.164 79	29.019 41	14.381 ± 0.002	13.326 ± 0.002	10.76 ± 0.05	7551	2.591	63.7
GMP2374	8128	195.233 59	27.790 85	13.610 ± 0.002	12.378 ± 0.002	9.84 ± 0.04	8251	2.733	34.5
GMP1900	8140	195.430 72	29.044 66	14.286 ± 0.002	13.332 ± 0.002	10.72 ± 0.04	7357	2.667	77.5
GMP1657	221460	195.517 50	29.253 45	14.590 ± 0.002	13.344 ± 0.002	10.59 ± 0.03	7573	2.679	78.5
–	8161	195.871 17	26.550 50	14.750 ± 0.002	13.651 ± 0.002	11.13 ± 0.04	6945	2.584	65.2
GMP0455	230051	196.110 60	27.304 31	15.328 ± 0.003	14.933 ± 0.004	13.53 ± 0.16	5766	2.344	46.2
–	8194	196.572 06	29.063 18	13.942 ± 0.002	12.746 ± 0.002	10.25 ± 0.03	7309	2.670	61.0
–	8195	196.594 62	29.657 53	16.496 ± 0.007	15.756 ± 0.010	12.66 ± 0.12	7296	2.391	81.2
–	8209	196.928 40	24.810 60	14.346 ± 0.002	13.390 ± 0.002	11.41 ± 0.05	6599	2.480	45.4
–	8220	197.131 58	24.700 76	14.537 ± 0.002	13.275 ± 0.002	10.41 ± 0.04	7398	2.713	82.5
–	8229	197.225 79	28.183 90	14.205 ± 0.002	13.170 ± 0.002	10.46 ± 0.08	6248	2.590	56.7
–	230117	197.238 22	28.280 51	15.761 ± 0.004	15.124 ± 0.005	12.90 ± 0.19	6108	2.332	54.5
–	8244	197.467 13	28.382 44	15.505 ± 0.004	14.730 ± 0.004	12.71 ± 0.13	7358	2.413	66.8
–	230139	197.698 53	29.709 90	14.912 ± 0.003	13.954 ± 0.003	11.82 ± 0.12	6619	2.461	48.6
–	8294	198.242 82	31.258 62	14.894 ± 0.003	14.262 ± 0.004	–	6320	2.386	53.0
–	8300	198.362 29	27.802 37	13.368 ± 0.002	12.079 ± 0.002	9.71 ± 0.03	6673	2.784	57.7
–	8317	198.598 35	30.483 99	14.790 ± 0.003	14.021 ± 0.003	11.94 ± 0.09	6287	2.473	66.4
–	8328	198.856 62	27.303 23	16.044 ± 0.005	15.333 ± 0.006	–	6740	2.405	73.8
–	8366	199.784 32	28.506 92	13.720 ± 0.002	12.710 ± 0.002	10.07 ± 0.06	6900	2.729	74.0

[a]Two further galaxies are Coma cluster members in Springob et al (2007), but removed from our spiral sample: (1) AGC8076, at a cluster-centric radius >2 Mpc and by far the lowest $cz = 2788$ km s^{-1}, is almost certainly a foreground galaxy; (2) GMP1582, at a radius of ∼1 Mpc and $cz = 9214$ km s^{-1}, is likely to be in the background. GMP1582 is also ∼0.5 mag fainter than any other source in our sample, and exhibits a clumpy, irregular morphology, causing large uncertainties in the photometry.

Table B2. TFR parameters for the Coma spiral galaxy sample introduced in Section 4.2. Columns as in Table 6. δM_X includes 0.12 mag uncertainty from the assumption that every galaxy is at the same line-of-sight distance as the cluster mean.

GMP ID	U/AGC ID	Δd_{CC} (Mpc)	Σ (Mpc^{-2})	$E(B-V)$	M_g (mag)	M_i (mag)	M_{K_s} (mag)	V_c (km s^{-1})
–	7845	6.81	14	0.015	−20.32 ± 0.12	−20.89 ± 0.12	−22.84 ± 0.17	135 ± 1
–	7877	6.39	11	0.015	−19.93 ± 0.12	−20.82 ± 0.12	−23.26 ± 0.17	158 ± 1
–	7890	6.16	3	0.017	−20.49 ± 0.12	−21.06 ± 0.12	−23.12 ± 0.17	156 ± 6
–	7955	5.13	5	0.015	−20.55 ± 0.12	−21.53 ± 0.12	−23.96 ± 0.16	180 ± 2
–	221022	4.63	9	0.013	−20.55 ± 0.12	−21.59 ± 0.12	−24.41 ± 0.15	174 ± 26
–	221033	4.87	2	0.011	−20.39 ± 0.12	−21.31 ± 0.12	−23.92 ± 0.16	158 ± 5
–	8004	6.31	4	0.014	−20.61 ± 0.12	−21.16 ± 0.12	−22.67 ± 0.16	151 ± 1
–	8013	3.36	7	0.012	−20.67 ± 0.12	−21.24 ± 0.12	−23.08 ± 0.18	177 ± 1
–	8025	3.42	2	0.019	−21.59 ± 0.12	−22.53 ± 0.12	−25.03 ± 0.15	247 ± 1
GMP5422	221130	1.68	28	0.010	−19.89 ± 0.12	−20.74 ± 0.12	−22.71 ± 0.20	108 ± 4
GMP5234	221147	1.83	46	0.010	−20.02 ± 0.12	−21.11 ± 0.12	−23.61 ± 0.16	164 ± 6
GMP5197	221149	1.93	8	0.010	−20.32 ± 0.12	−21.20 ± 0.12	−23.44 ± 0.16	151 ± 8
GMP5006	8069	2.03	17	0.012	−21.03 ± 0.12	−22.03 ± 0.12	−24.44 ± 0.15	194 ± 13
–	221174	2.56	15	0.016	−20.40 ± 0.12	−21.24 ± 0.12	−23.70 ± 0.16	167 ± 7
GMP4437	221206	1.37	11	0.013	−20.21 ± 0.12	−21.16 ± 0.12	−23.59 ± 0.16	131 ± 1
GMP3896	8096	0.41	284	0.014	−20.99 ± 0.12	−21.64 ± 0.12	−24.23 ± 0.15	182 ± 8
GMP2987	8108	1.77	21	0.010	−21.49 ± 0.12	−22.38 ± 0.12	−24.60 ± 0.15	206 ± 7
GMP2582	221402	0.71	120	0.010	−19.57 ± 0.12	−20.50 ± 0.12	−23.19 ± 0.16	132 ± 7
GMP2559	221406	0.32	171	0.011	−19.89 ± 0.12	−20.54 ± 0.12	−23.36 ± 0.16	134 ± 8
GMP2544	8118	1.76	12	0.014	−21.05 ± 0.12	−21.96 ± 0.12	−24.42 ± 0.16	195 ± 3
GMP2374	8128	0.49	169	0.008	−21.59 ± 0.12	−22.76 ± 0.12	−25.27 ± 0.15	270 ± 13
GMP1900	8140	1.90	19	0.017	−21.47 ± 0.12	−22.17 ± 0.12	−24.52 ± 0.15	232 ± 1
GMP1657	221460	2.27	14	0.012	−21.19 ± 0.12	−22.17 ± 0.12	−24.65 ± 0.15	239 ± 12
–	8161	2.70	2	0.013	−20.69 ± 0.12	−21.64 ± 0.12	−24.05 ± 0.16	192 ± 1
GMP0455	230051	2.01	7	0.013	−19.84 ± 0.12	−20.18 ± 0.12	−21.60 ± 0.22	110 ± 9
–	8194	2.95	19	0.011	−21.50 ± 0.12	−22.55 ± 0.12	−24.92 ± 0.15	234 ± 5
–	8195	3.65	7	0.012	−18.91 ± 0.12	−19.50 ± 0.12	−22.58 ± 0.19	123 ± 4
–	8209	6.00	1	0.017	−20.88 ± 0.12	−21.76 ± 0.12	−23.71 ± 0.16	151 ± 6
–	8220	6.32	2	0.022	−21.41 ± 0.12	−22.35 ± 0.12	−24.83 ± 0.16	258 ± 1
–	8229	3.32	18	0.015	−21.15 ± 0.12	−22.06 ± 0.12	−24.69 ± 0.17	195 ± 8
–	230117	3.35	36	0.010	−19.42 ± 0.12	−19.99 ± 0.12	−22.24 ± 0.24	107 ± 7
–	8244	3.71	27	0.009	−19.79 ± 0.12	−20.46 ± 0.12	−22.47 ± 0.20	129 ± 1
–	230139	4.87	3	0.013	−20.31 ± 0.12	−21.19 ± 0.12	−23.31 ± 0.19	145 ± 5
–	8294	7.16	2	0.012	−20.31 ± 0.12	−20.87 ± 0.12	–	122 ± 5
–	8300	4.98	5	0.017	−22.13 ± 0.12	−23.25 ± 0.12	−25.44 ± 0.15	304 ± 5
–	8317	6.65	8	0.014	−20.57 ± 0.12	−21.21 ± 0.12	−23.24 ± 0.17	149 ± 2
–	8328	5.83	2	0.011	−19.31 ± 0.12	−19.89 ± 0.12	–	127 ± 1
–	8366	7.07	2	0.019	−22.04 ± 0.12	−22.79 ± 0.12	−25.14 ± 0.16	268 ± 1

This paper has been typeset from a TEX/LATEX file prepared by the author.